Exploring the Limits of Multiplexing Kinetic Inductance Detectors

Hessel Schulte

Delft University of Technology

TU Delft

Exploring the Limits of Multiplexing Kinetic Inductance Detectors

by

Hessel Schulte

to obtain the degree of Master of Science in Applied Physics
at the Delft University of Technology,
to be defended publicly on Thursday December 12th, 2024 at 12:00

Student number:	4862791	
Project duration:	March 18 2024 – December 12, 2024	
Daily Supervisor:	Wilbert G. Ras	
Thesis committee:	Prof. Dr. Ir. Jochem J.A. Baselmans	TU Delft/SRON, supervisor
	Dr. Pieter J. de Visser	SRON, Supervisor
	Dr. Mazhar N. Ali	Kavli, TU Delft

An electronic version of this thesis is available at http://repository.tudelft.nl/.

TU Delft

Acknowledgements

First of all, the front cover of this thesis is AI generated and is only meant to entice the reader. The image does not reflect any real telescope design.

Second it must be mentioned that any successes this thesis achieved can not only be credited to me but at least as much to everyone at the the Terahertz Sensing group and the clean room engineers who have spent years improving KID designs, fabrication methods and readout equipment to the level where they are now. The expertise and effort required before a master student can come in and do the experiments I did is not lost on me.

More specifically I would like to thank David for helping me better understand the fabrication of KIDs, for enthusiastically bringing in new ideas during insightful meetings throughout the whole thesis and of course for flawlessly realising every design we gave him. Thanks to Martijn for letting me take up whole afternoons for making SEM images. We had some nice conversations during these repetitive tasks. Thanks to Pieter for assisting me a little bit in getting an internship at JPL approved. I very much look forward to moving to Los Angeles to do more experimental work on KID devices. Thanks to Wilbert for guiding the project, for being patient with me, for mentioning when work was inadequate and to do so in time before problems became too big to overcome. It was often needed. Our Tuesday meetings were always useful and every time I walked away with a clearer idea of what to do next. I will also give thanks to the Terahertz Sensing group as a whole for providing a warm and open atmosphere where anyone can quickly become a part of the group.

Finally, I express my gratitude towards my family for supporting me all the way through my academic career which included an inspiring year as part of the TU Delft Hydro Motion team, which would not have been possible without your support, as well as two not so inspiring years of a pandemic. Thank you for so fully entrusting me with decisions for my studies and believing that I am indeed working on useful stuff. Also to my friends at DPC, weekly evenings with you were always a nice distraction and helped to clear my mind no matter everyone's stress level, except on Thursdays.

As I am about to end my studies with a thesis and an internship delving into one of the most niche areas of electronics and physics I can personally imagine, some people have asked me why I chose to study physics in general, but also why I would choose a subject with such limited day-to-day applications. I am often reminded of a quote that strongly resonates with me. It is attributed to Richard Feynman in a biography written by Ralph Leighton, a close friend of Feynman's, which has a sentiment I believe also lives in parts of the Terahertz Sensing group:

Physics is like sex. Sure, it may give some practical results, but that's not why we do it.

-Richard P. Feynman

Hessel Schulte
Delft, December 2024

Abstract

In the mission of understanding the origins of life on earth and in the universe, astronomers are looking to exoplanets for signs of life. The spectra of light that has passed through an exoplanet's atmosphere is analysed for biomarkers. Until now most exoplanets have been found and characterised using the transit method. In the coming decade the aim is to look for planets using direct detection methods. In part for this purpose the European Extremely Large Telescope (EELT) is currently under construction and in future the Habitable World Observatory (HWO) is planned as a space-based telescope. To make full use of the EELT and the WHO extreme adaptive optics (XAO) systems using wave front sensors and deformable mirrors are needed. Contemporary CCD cameras utilizing semiconductor band gap energies are not sufficiently sensitive for wavefront sensing in direct exoplanet detection, let alone perform measurements to characterise their atmospheres. To this end different detectors are needed.

Kinetic inductance detectors (KIDs) are promising superconducting, energy resolving devices capable of single photon detection in the near-infrared and visible regimes. Another often cited advantage of KIDs is that, in theory, many detectors can easily be coupled to a single set of readout electronics. To make devices capable of producing images comparable to those achieved with CCDs we need a similar amount of pixels. The largest KID arrays to date are in the order of a thousand pixels on one readout line, whereas CCDs have in the order of millions of pixels. In this thesis some theoretical and practical limits on KID multiplexability while retaining high pixel yield are explored.

Currently, frequency scatter is the most limiting issue on increasing the MUX factor. A tool is created to determine yield criteria for KID arrays. The response of KIDs to absorption of photons with a certain energy is modelled using an effective temperature change in the inductor. From this model a criterion for minimal frequency spacing between KIDs on an array df_0 = $0.94\,\mathrm{MHz}$ is extracted for KIDs with Q = 5.0×10^4. On a 4-$8\,\mathrm{GHz}$ bandwidth, and a <-$10\,\mathrm{dB}$ cross talk criterion, this results in a theoretical maximum MUX factor of 4264. Assuming a normal distribution of fabricated resonance frequencies around the designed frequencies we calculate the maximum tolerable frequency scatter to be $\sigma_{\delta \mathrm{f}/\mathrm{f}}$ = 0.2×10^{-3} for a 1000 pixel array.

Before post-processing a frequency scatter of $\sigma_{\delta \mathrm{f}/\mathrm{f}}$ = 3.9×10^{-3} is measured in a 400 pixel, 4.1-$7.9\,\mathrm{GHz}$ bandwidth array. Some possible sources of scatter are investigated. Lithographic fabrication tolerances on detector dimensions are shown to partially explain the observed value. A boundary effect is also observed in the array which has raised the calculated f-scatter. We aimed to prove to prove that high yield, 1000 KID arrays are possible with a post-processing experiment. With this experiment we attempted to lower f-scatter in the array. After post-processing, a scatter of $\sigma_{\delta \mathrm{f}/\mathrm{f}}$ = 0.21×10^{-3} is achieved, representing an improvement of nearly a factor 18. The new $\sigma_{\delta \mathrm{f}/\mathrm{f}}$ allows for array sizes of up to 980 KIDs on a single readout line with an expected yield of 95%.

Contents

Nomenclature

Abbreviations

Abbreviation	Definition
KID	Kinetic Inductance Detector
MKID	Microwave Kinetic Inductance Detector
LEKID	Lumped Element Kinetic Inductance Detector
VNA	Vector Network Analyser
NbTiN	Niobium-Titanium-Nitride
$\beta - \mathrm{Ta}$	Bèta-Tantalum
SEM	Scanning Electron Microscope
FWHM	Full Width Half Maximum
EBPG	Electron Beam Pattern Generation

Symbols

Symbol	Definition	Unit
$\mathrm{x_i}$	image distance	[m]
$\mathrm{x_o}$	object distance	[m]
f	Frequency	[Hz]
$\mathrm{f_0}$	Resonance frequency	[Hz]
$\mathrm{df_0}$	Frequency space between KIDs	[Hz]
$\mathrm{f_{lens}}$	Focal length of lenses	[m]
Q	Quality factor	[-]
$\mathrm{Q_c}$	Coupling quality factor	[-]
$\mathrm{Q_i}$	Internal quality factor	[-]
R	Resolving power	[-]
$\delta\mathrm{f}$	Frequency error	Hz
$\sigma_{\delta\mathrm{f/f}}$	Frequency scatter	[-]
σ_{Q}	Quality factor scatter	[-]
χ_{RL}^{col}	Crosstalk of right KID on left KID due to frequency collisions	[dB]
$\phi_{\mathrm{L}}^{R_{dark}}$	Phase of left KID at resonance with a dark right neighbour	[Rad]
$\phi_{\mathrm{L}}^{R_{exc}}$	Phase of left KID at resonance with an excited right neighbour	[Rad]

1

Introduction

1.1. Exoplanet discovery

Throughout history there have been many theories concerning the origins of life as we know it. Not many theories have provided satisfactory answers and many live in the realm of the philosophical or the unverifiable. In the mission of understanding how life came to be, both on Earth and in the universe, a good place to start is to wonder what conditions are needed for life to exist. We look outward to planets orbiting other stars to answer the question 'Has life developed anywhere other than the Earth?'. The most obvious candidates for this search are Earth-like rocky planets in orbits within the habitable zones of their host star. To assess the likelihood of an exoplanet containing life, astronomers look for biomarkers. The presence of water, carbon dioxide and methane in the atmosphere are examples of such markers. Each of these gases will absorb specific wavelengths of light, creating spectral lines in spectra obtained from these planets. In figure 1.1 we see an example of what an Earth-like spectrum might look like[1].

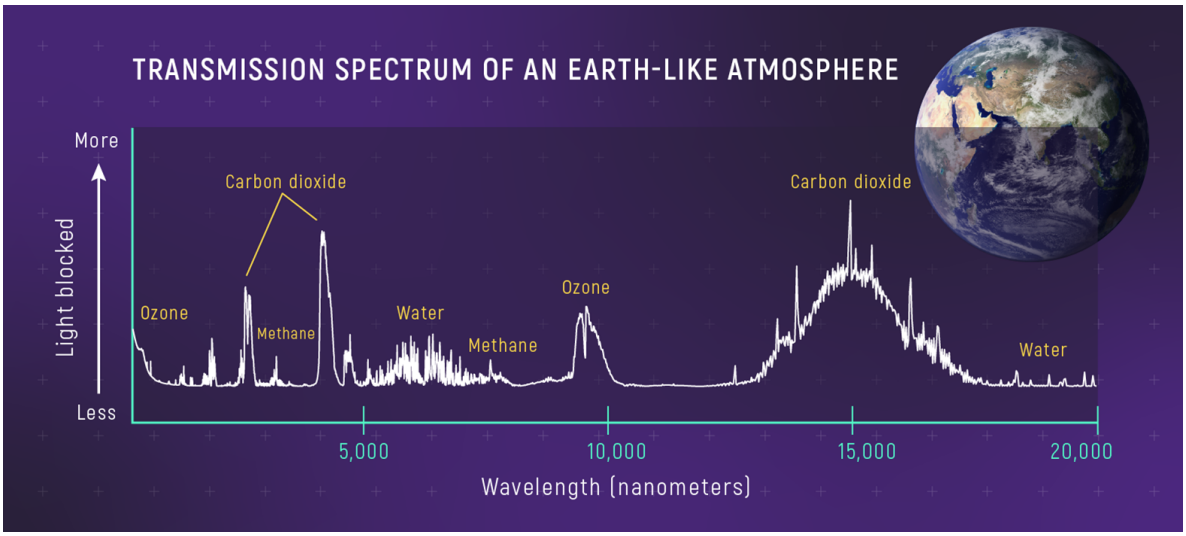

Figure 1.1: [1] A transmission spectrum of an earth-like atmosphere. The absorption of light by the biomarkers carbon dioxide, water, methane and ozone creates spectral lines at the indicated wavelengths.

To measure such a spectrum, an exoplanet needs to be located and light that has passed through its atmosphere needs to be caught. To date, most exoplanets have been detected using the 'transit method' where a decrease in a star's brightness due to an orbiting planet blocking part of its light is measured. In recent years some exoplanets have also been detected with the 'direct method' which uses a host star's reflected light off of a planet. The advantage of the direct method is that all captured

light will have passed through a planet's atmosphere, whereas with the transit method, the light captured directly from the star needs to be filtered out. The spectra of transit observation can be compared to the spectrum of the bare star [2]. This makes data tricky to analyse. The downside of the direct method is that the signal is extremely faint. In fact we can expect to receive only between 1 and 50 photons per hour per $1\,\mu\mathrm{m}$ bandwidth [3]. In the coming decade our ability to characterise exoplanets will be greatly improved by the European Extremely Large Telescope (EELT) and later by the Habitable Worlds Observatory (HWO). Construction of the EELT is well under way with first light expected in 2028 as of the completion of this thesis. When finished, it will be the largest telescope in the world capable of visible and near infra-red (NIR) observations.

Because exoplanets are such faint sources we need single-photon sensitive light detection [3]. Using ground-based telescopes like the EELT, turbulence in the earth's atmosphere will distort our images. To combat these distortions we also have a need for highly sensitive wavefront sensors [4]. Paired with deformable mirrors, a wavefront sensor can correct for atmospheric distortions in real time. This is called adaptive optics (AO) and in future wavefront sensors with higher pixel counts will be required [4] for extreme adaptive optics systems (XAO). Currently semiconductor based CCD detectors are used in AO. In these detectors photons above the bandgap energy (in the order of $1\,\mathrm{eV}$) can excite an electron and from the collected charge over time, the intensity of a source can be measured [5]. CCDs also require filtering of incoming light to determine a colour [6] meaning many photons are needed before an accurate image can be produced. For the purpose of direct exoplanet detection CCDs are not sensitive enough.

1.2. Superconducting photon detectors

As an alternative to semiconductor based technologies, some superconducting photon detectors have been proposed for use as wavefront sensors. Kinetic Inductance Detectors (KIDs) are superconducting photosensitive devices with bandgap energies in the order of $1\,\mathrm{meV}$, capable of single-photon counting for NIR and visible light [7]. These detectors are also energy resolving so from the absorption of just one photon information can be gathered about its position, time of arrival and frequency at the same time. Functionally KIDs are easily described by the electrical diagram in figure 1.2 (a) with a capacitor and a photosensitive inductor coupled to a readout line. As such a KID is simply a superconducting LC resonator that will block the transmission of signals in the readout line at its resonance frequency f_0. In figure 1.2 (b) The transmission of a signal with a range of readout frequencies through the transmission line is plotted. This dip is caused by a resonator with an f_0 of $4.04\,\mathrm{GHz}$

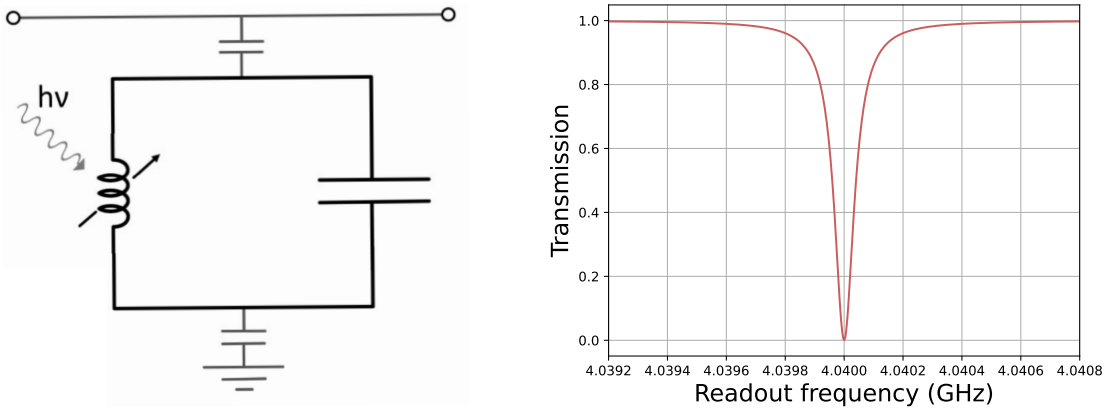

(a) (b)

Figure 1.2: Left [8] shows an electrical diagram of an LC resonator representing a KID. In these arrays every resonator is capacitively coupled to the transmission line. The arrow over the inductor indicates variable impedance when absorbing a photon with energy $\mathrm{h}\nu$. Right graph showing how the transmission of a signal is blocked by a resonator around a resonance frequency f_0 = $4.04\,\mathrm{GHz}$

KIDs can be fabricated with a wide range of inductances, capacitances and resonance frequencies. Coupling KIDs to the same readout line makes them intrinsically easy to multiplex to one set of readout electronics. Several KIDs coupled to the same transmission line will be referred to as an array. Figure 1.3 shows an array made up of 400 KIDs used throughout this thesis. The detectors in this image are so-called Lumped Element KIDs (LEKIDs). These are compact detectors [9] which allow for such array designs with high filling factors. The multiplexability together with single-photon counting capabilities make KIDs an ideal candidate for wavefront sensing. Making use of energy resolving capabilities adds the benefit of spectrally resolving the wavefront without the need for filters or gratings that spread light over the array and reduce throughput.

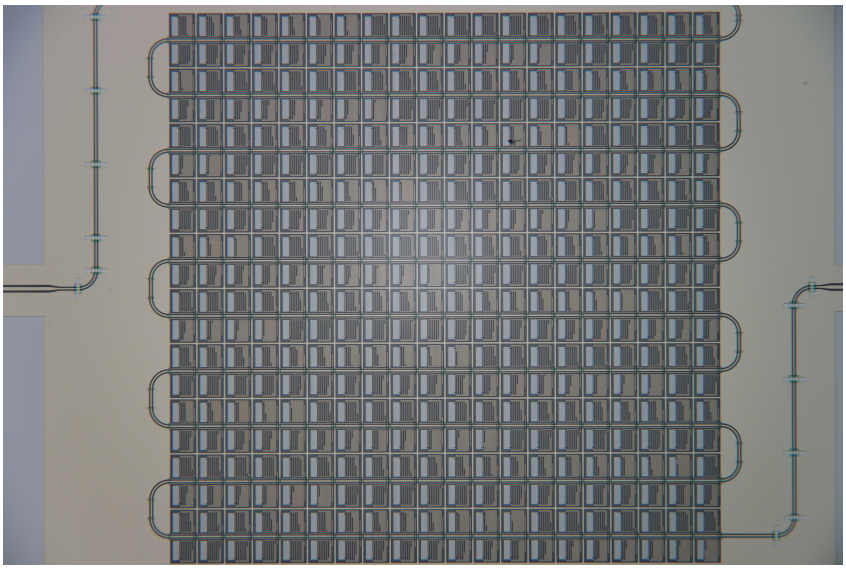

Figure 1.3: A 400 pixel LEKID array labelled as 'LT361' imaged under an optical microscope. Every coloured square is a KID, the meandering line is the throughline all KIDs are coupled to. The throughline exits the image on the right and left side where it will be connected to readout electronics.

1.3. Frequency scatter

To make AO systems of the quality achieved with CCDs, a KID device needs a comparable number of pixels, where every resonator is counted as a pixel. CCDs can have arrays of millions of pixels whereas the largest KID arrays have in the order of a thousand pixels [10] on one readout line. The MUX factor in our arrays needs to be significantly increased to be competitive. While we can indeed multiplex as many KIDs to the same readout electronics as we want, not all of them may be usable. In figure 1.2 (b) we see the transmission dips have a finite width. Due to inevitable losses in the resonator there is a limit to how narrow we can make these dips. If the dips of two or more resonators overlap our ability to measure their response to a photon will be impeded. The fraction of pixels that are considered usable is the yield of an array. The mentioned large KID arrays currently have a yield of <$90\,\%$[10]. We only have so much room to place all KIDs in frequency space. In the arrays we look at here, we are limited to a bandwidth of 4-$8\,\mathrm{GHz}$. This raises the first question we aim to answer in this thesis:

What is the theoretical limit on the MUX factor in single readout line KID devices while retaining a $100\,\%$ yield?

Besides the theoretical limits on array sizes and yield resulting from a finite bandwidth and transmission dip width in, in practice we are faced with other limits on array yield. The array in figure 1.3 is designed to have a constant frequency spacing df_0 of $9\,\mathrm{MHz}$ between all transmission dips. The top graph in figure 1.4 shows the full transmission of the whole 400 KID array. Every dip in this graph is denoted by a blue triangle and represents one KID. These dips can not be placed perfectly in frequency space.

That much becomes clear from the bottom graph of figure 1.4 where we zoom in on a small segment of the transmission graph. We observe big differences in frequency spacing over the array.

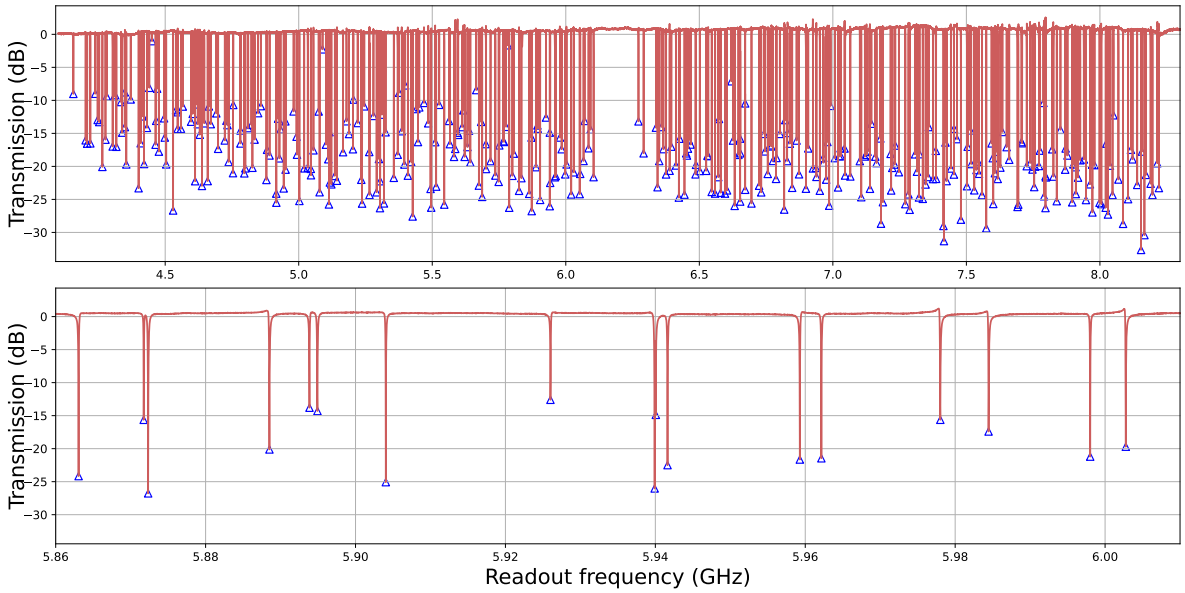

Figure 1.4: Top graph showing the transmission of the full 400 pixel array in figure 1.3. Bottom graph showing a smaller bandwidth highlighting imperfect placement of KIDs in the frequency domain. Counted dips are marked by blue triangles.

The error in resonance frequencies compared to a perfect array is called the frequency scatter of f-scatter. It causes some transmission dips to overlap as we see in figure 1.4. Frequency scatter is currently by far the biggest hurdle in achieving high yield in arrays with more than a few hundred KIDs. The resonance frequencies must be gotten under control if KIDs are to be used in XAO in the future. There are some suspected causes of f-scatter like inaccurate array fabrication, electromagnetic effects between KIDs and effects of the measurement setup itself. In literature others have been able to significantly reduce frequency scatter by post-processing KIDs [11]. We will attempt to do the same, leading to the second question to be answered in this thesis:

How much can array yield be improved using post-processing techniques?

For this thesis we set the goal to enable fabrication of arrays with 1000 KIDs per readout line on a $4\text{-}8\,\mathrm{GHz}$ readout bandwidth with a >95% yield criterion.

1.4. Thesis outline

The report starts with theoretical background information on kinetic inductance detectors and their properties, including an explanation on how to model KID response. From that model yield criteria for KID arrays of a certain size are determined. The fabrication process of KID arrays is described in chapter 3. Scanning Electron Microscope (SEM) images are made and a method for determining fabrication tolerances is described. The tolerance is translated to an f-scatter. Chapter 4 gives an overview of the experiments performed. Here a method for accurately calculating f-scatter and yield is discussed. We put an emphasis on work done on post-processing experiments. In chapter 5 the results from previous chapters and some concise comments on their meaning are given. Chapter 6 will then discuss implications of the results in more detail as well as some suggestions for future research on large optical KID arrays. Finally, the conclusions drawn from the experiments and analysis are presented at the end, in chapter 7.

2

Theoretical background

2.1. Kinetic inductance detectors

Detectors relevant to this thesis specifically are lumped element KIDs (LEKIDs) . One of these LEKIDs within a larger array is shown in figure 2.1 as seen through an optical microscope. KIDs are built up from three components: an inductor which absorbs photons, an interdigitated capacitor (IDC) which will be important to decide certain properties of a KID in the design, and a coupler bar to transmit signals to and from the transmission line. Coupler bars are directly connected to the transmission line through a bridge over the ground plane, visible as grey planes in figure 2.1. This ground plane fills any empty space between KIDs and alongside the transmission line. Note how the KIDs themselves are not connected to a common ground plane. Experiments with grounded KID arrays were also conducted, however these did not show promising results so here we consider floating ground KID arrays. In figure 2.1 the KID is surrounded by a dark grey plane, this space is unfilled by any metal so the bare sapphire wafer substrate is shown. The empty space is used to isolate KIDs from the ground plane.

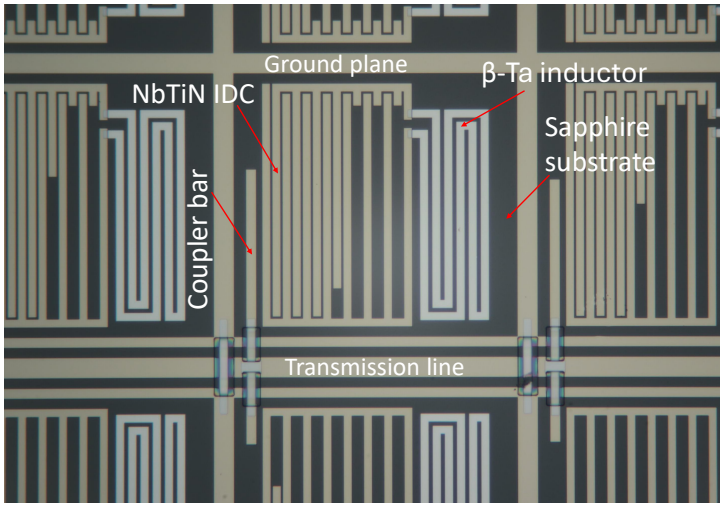

Figure 2.1: Optical microscope image of a lumped element KID in a larger array. The dark grey areas are parts of the sapphire substrate, light grey structures are $\beta - \mathrm{Ta}$ inductors. The IDCs, coupler bars, transmission line and ground plane indicated in the image are all NbTiN.

Every KID is essentially nothing more than an LC resonator coupled to a transmission line with an incoming AC signal. It is because of the fact that many different KIDs can be simply coupled to the same transmission line that we can in theory easily multiplex many of them on the same readout equipment. LC resonators have a certain resonant frequency f_0 which is, as the name suggests, dependant on the capacitance and inductance of the resonator. KIDs will only resonate with the signal being driven in

the transmission line if the signal contains the correct frequency f_0. This principle will be used to find and perform measurements on arrays of KIDs, each with their own f_0.

As mentioned in chapter 1 semi-conductor based detectors can not be sufficiently sensitive to detect single photons in the optical regime. Instead superconductive metals which have a much smaller band-gap energy Δ are needed with some measurable property change as a photon is absorbed. The materials used become superconducting when cooled to near absolute zero. Specifically these materials are Bèta-Tantalum ($\beta - \mathrm{Ta}$) for the inductors and Niobium-Titanium-Nitride (NbTiN) for the capacitors, coupler bars and throughline. In superconducting metals, lattice vibrations of atoms are so low that electrons in the inductor are able to bind and form so-called Cooper pairs [12]. Absorption of a photon of a photon in the inductor will break a certain number of cooper pairs into quasi-particles which can indirectly be measured to determine what the energy of the photon was.

During an actual measurement where photons are absorbed we cannot count the number of quasi-particles that are created by each photon directly. Instead the transmission of the signal through the array is continuously measured. A modelled example of a transmission curve of a single KID with an f_0 of $4.04\,\mathrm{GHz}$ is shown in figure 2.2 (a). This curve is only the real part of the transmission which can be directly measured during real experiments. In section 2.2 we will mathematically see that there is also an imaginary component to the transmission. Interestingly if the imaginary and real components of resonator transmission are plotted against each other, it creates a resonance circle as is seen in figure 2.2 (b). This circle is used to define a phase θ which is important in reading out KID response. A KID resonates only with signals very close to its f_0 where it will reflect the signal and indeed a transmission of 0 is seen in figure 2.2(a). Far away from resonance the signal is fully transmitted, creating the observed transmission dip. When a photon is absorbed this dip will get wider and shift towards lower frequencies. A detailed explanation of this is given in section 2.2.

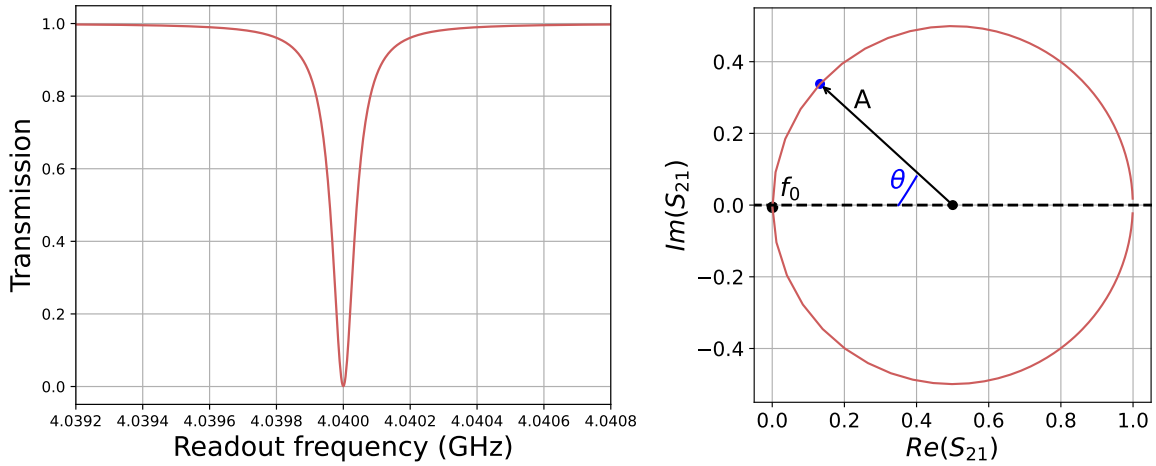

Figure 2.2: Left graph showing an example of a transmission dip of a dark KID at the low end of the readout frequency spectrum. Right figure showing the resonance circle of the same KID with amplitude A and phase θ indicated

Transmission dips have a characteristic shape which will be analysed extensively to characterise KIDs. First of all the width of dips are quantified with the dimensionless quality factor Q defined by equation 2.1. This Q is not the only factor determining the shape of transmission dips, in practice asymmetry in dips are also observed. Asymmetry is especially relevant at higher frequencies and will be further discussed in section 4.2.

$$Q = \frac{f_0}{FWHM} \tag{2.1}$$

Where FWHM is the Full Width Half Maximum, defined as the bandwidth between the two points on the dip with a transmission of 0.5. The arrays relevant to this thesis have been designed to have a constant Q of 5.0×10^4 meaning KIDs at higher frequencies will, in absolute sense, have broader transmission dips than KIDs at lower frequencies.

Due to unavoidable losses in a resonator, transmission dips always have a finite width. Because of that fact there is a limit to how many KIDs fit on a certain bandwidth without them overlapping. Designing and fabricating a KID to have the exact f_0 that was intended is difficult and many finite element simulations have been performed to make KID designs with accurately predictable properties [13][14]. Simulations are focussed on varying IDC finger lengths and coupler bar lengths in order to adjust the f_0 of KIDs. Inductors cannot be changed and should be identical for all KIDs. Changing the volume of inductors will have a significant effect on the response of a KID to absorbing a photon. Ideally every KID has an identical response to photons of the same energy, so calibration of energy readout can be done once for the whole array. The SONNET software was used to design arrays and to estimate resonance frequencies and quality factors of all KIDs. Simulations are run for discrete steps in IDC finger and coupler bar lengths to save on computing time. Interpolation is then used on the simulated length values to design KIDs with the desired properties. Figure 2.3 shows the measured resonance frequencies of a fabricated, 400 KID array plotted against the designed resonance frequencies. The measured resonance frequencies are scattered about a line in this graph defined by a least square fit through the data points. A larger shift in measured resonance frequencies is also observed by how the data points do not move over a $\mathrm{f}_0^{measured} = \mathrm{f}_0^{design}$ line. We are less interested in this shift as yield of an array is determined by the frequency spacing df_0 between KIDs. The scattering around the fit is a much bigger issue for the yield.

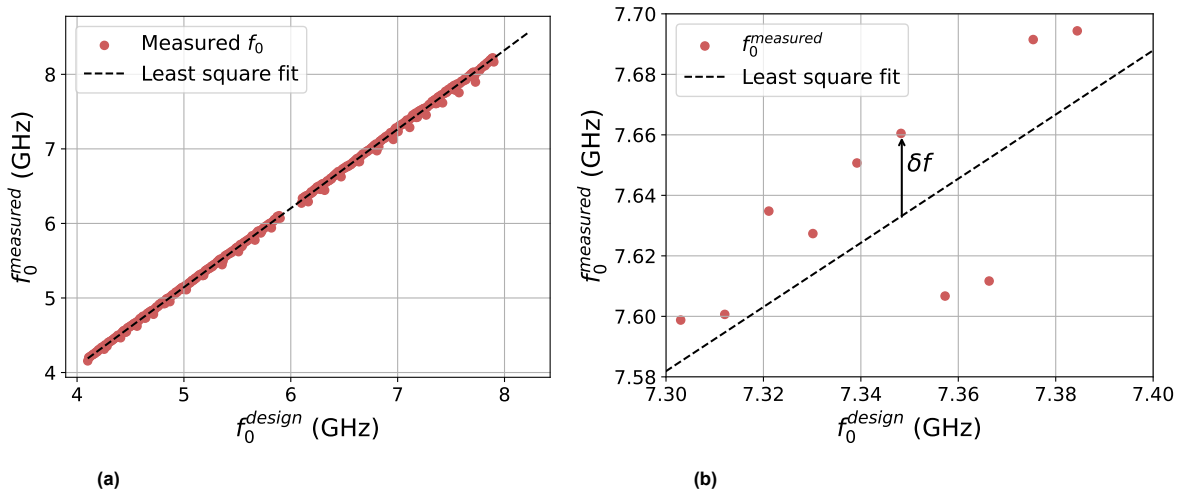

Figure 2.3: Left image showing the measured resonance frequencies in a 400 KID array plotted against the designed resonance frequencies The dashed black line shows a least square fit through the data. Right image showing a zoomed in image of the same plot. We define a frequency error $\delta\mathrm{f}$ as the difference between a measured resonance frequency and the fit. The frequency scatter of one KID $\delta\mathrm{f}/\mathrm{f}$ is the frequency error normalised by the resonance frequency of that KID.

To define frequency scatter concretely,figure 2.3 (b) zooms in on a smaller segment of the graph in figure 2.3 (a). In a completely scatter-free array every measured resonance frequency would be positioned on the dashed black line. Instead KIDs have a frequency error $\delta\mathrm{f}$, defined as the distance between the resonance frequency and the least square fit. To be able to compare errors over the whole array the errors are normalised by the resonance frequency of the respective KIDS. Frequency scatter $\sigma_{\delta\mathrm{f}/\mathrm{f}}$ of an array is determined by calculating the standard deviation of all frequency errors. A larger f-scatter will result in some KIDs moving very close together in frequency space. In some cases causing the dips to overlap. As KIDs get hit with photons their dips will shift, effectively making their resonance frequency change over time. Precisely why overlapping dips are a problem will be discussed later in section 2.2.

The array was designed to have a constant frequency spacing $\mathrm{df_0}$ of $9\,\mathrm{MHz}$ between all KIDs. SONNET simulations can not be expected to account for all effects that have an impact of the true $\mathrm{f_0}$ of a resonator. Also imperfections in fabrication, material properties and electromagnetic cross talk in an array may change KID properties.

2.2. KID response model

To better describe overlap between transmission curves and quantify the change in $\mathrm{df_0}$ over time that can be expected, a mathematical description of transmission dips and KID response is needed. As said before the inductance of a KID changes when an incoming photon breaks cooper pairs. Since we cannot directly measure the number of quasiparticles in an inductor, a model based on an effective temperature change in the inductor is used [15]. A change in KID temperature also changes the quasiparticle density in an inductor. Since the bandgap energy Δ of our superconductor is known, effective temperature can be correlated to the energy of an incoming photon through KID response.

The effects of a changing effective temperature on a KID can be expressed by a change in complex conductivity $\sigma = \sigma_1 - i\sigma_2$. The following section will describe how this is used to create an accurate response model. First the complex conductivity at some temperature T is calculated according to Mattis-Bardeen theory [16]

$$\frac{\sigma_1}{\sigma_N} = \frac{2}{\hbar\omega}\int_{\Delta}^{\infty}[f(E) - f(E+\hbar\omega)]g_1(E)dE + \frac{1}{\hbar\omega}\int_{min(-\Delta,\Delta-\hbar\omega)}^{-\Delta}[1-2f(E+\hbar\omega)]g_1(E)dE \tag{2.2}$$

$$\frac{\sigma_2}{\sigma_N} = \frac{1}{\hbar\omega}\int_{max(-\Delta,\Delta-\hbar\omega)}^{\Delta}[1-2f(E+\hbar\omega)]g_2(E)dE \tag{2.3}$$

Where $f(E, k_bT)$ notates the Fermi-Dirac distribution of quasiparticles with energy E and temperature T and σ_N is the so-called normal state conductivity of a material in its non superconductive state. Notice how in 2.2 the second integral is only non-zero when $\hbar\omega > 2\Delta$. In other words, this term only contributes when the absorbed energy is greater than the band gap so that Cooper pairs are broken. Lastly the energy and band-gap dependencies $g(E)$ are given in 2.4 and 2.5. Note that the two expressions are very similar, and related by $g_2(E) = -i \cdot g_1(E)$.

$$g_1(E) = \frac{E^2 + \Delta^2 + \hbar\omega E}{\sqrt{E^2-\Delta^2}\sqrt{(E+\hbar\omega)^2-\Delta^2}} \tag{2.4}$$

$$g_2(E) = \frac{E^2 + \Delta^2 + \hbar\omega E}{\sqrt{\Delta^2-E^2}\sqrt{(E+\hbar\omega)^2-\Delta^2}} \tag{2.5}$$

The complex conductivities calculated at different T are then used to find kinetic inductances L_k and internal quality factors Q_i. Q_i represents energy losses in the KIDs.

$$L_k = \mathrm{im}\left(\frac{1}{\sigma_1 - i\sigma_2}\right)\frac{1}{2\pi f_0} \tag{2.6}$$

$$Q_i = \frac{2}{\alpha_k\beta}\frac{\sigma_2}{\sigma_1} \tag{2.7}$$

Here two factors that characterise KIDs are introduced. The fraction α_k of total inductance L which is contributed to kinetic inductance and β, a factor dependant on the ratio between film thickness d and magnetic penetration depth λ: $\beta = 1 + \frac{2d/\lambda}{sinh(2d/\lambda)}$. We take α_k=0.96 for all KIDs relevant to this thesis and all structures in our arrays can be seen as thin films so $\beta = 2$. Assuming the coupling quality factors $\mathrm{Q_c}$ are known the measurable total quality factor Q is found.

$$\frac{1}{Q} = \frac{1}{Q_i} + \frac{1}{Q_c} \tag{2.8}$$

To model a dark KID in fact only the known resonance frequencies and the quality factors which were just calculated are needed [17]. The dark transmission S_{21} is calculated by 2.9. The real component of this is in fact results in a transmission dip as is seen in figure 2.2 and from there resonance circles, phase diagrams etc. are easily acquired.

$$S_{21} = \frac{Q/Q_i + 2i\frac{\delta\omega}{\omega_0}}{1 + 2iQ\frac{\delta\omega}{\omega_0}} \tag{2.9}$$

Where ω_0 is the angular resonance frequency and $\delta\omega$ is the frequency distance from resonance at any point on the transmission curve. Equation 2.9 is also used to calculate curves of excited KIDs and since complex conductivity may be found for any effective temperature as long as we are in the clean or dirty limit [15] the new quality factors are already known. To find the new resonance frequency some additional steps are required. We use the fact that capacitance C of a KID remains unchanged as it gets hit by a photon. The value of C is extracted from the equation for the known initial resonance frequency f_0 in an LC resonator.

$$f_0 = \frac{1}{2\pi\sqrt{C\frac{L_k}{a_k}}} \tag{2.10}$$

Kinetic inductance, like the quality factor, is calculated with complex conductivity which is known for different effective temperatures. Now that C is known, the response resonance frequency is found by substituting $\mathrm{L_k}$ for the relevant temperature in 2.10. with that the response values can be substituted in equation again in equation 2.9 to find a response transmission curve. An example of such a response from a high energy, blue photon compared to the dark transmission of the same KID can be seen in figure 2.4 together with the resonance circles in both situations. The decrease in amplitude of the dip is visible by the small radius and the dark resonance point f_0 has shifted over the circle as the dip shifted toward lower frequencies. This approach can be applied to model KID response for any resonance frequency on the readout bandwidth and any quality factor.

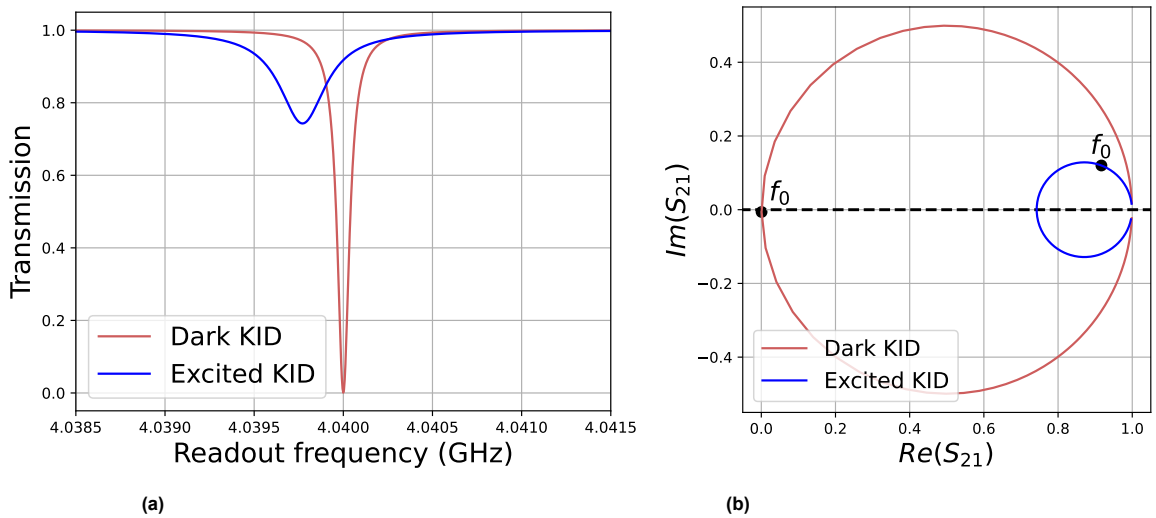

Figure 2.4: Left graph showing an example showing a dark KID (red) and a KID just hit with a photon (blue). Note the decrease in resonance frequency as well as quality factor from $\mathrm{Q_{dark}} = 5.0 \times 10^4$ to $\mathrm{Q_{excited}} = 1.3 \times 10^4$. Right image showing the resonance circles in the same situations. The phase at f_0 has changed as well as the amplitude of the whole circle.

If there are multiple KIDs on some bandwidth, a combined transmission curve is found by simply multiplying the separately calculated transmission curves of all KIDs or by adding them on a logarithmic

scale. This is only true for KIDs with no significant electromagnetic crosstalk, which introduces a cross-term to the transmission. Later, we will see array design is important for making this assumption valid. Even without EM-cross talk, at some point a problem arises when trying to multiplex more and more KIDs on a single array. Increasing array size means transmission dips will need to move closer together to fit all KIDs on the bandwidth. Figure 2.5 (a) shows two close frequency neighbours in unexcited state, we denote the left KID as 'A' and the right KID as 'B'. In figure 2.5 (b) KID B absorbs a photon and its dip moves towards A accordingly, changing the shape of both dips. The problem of having 2 KIDs so close in frequency becomes clear in figure 2.5 (c) by noting the difference between the dip shape of KID A in excited states with an excited or dark KID B. In practice photon energies are determined using phase change at the resonance of a KID, denoted by vertical dashed lines in the images. Figure 2.5 (d) then shows the significant difference in measured phase in KID A depending on B also being excited. In literature this effect of crosstalk due to overlapping transmission dips is referred to as a frequency collision [18].

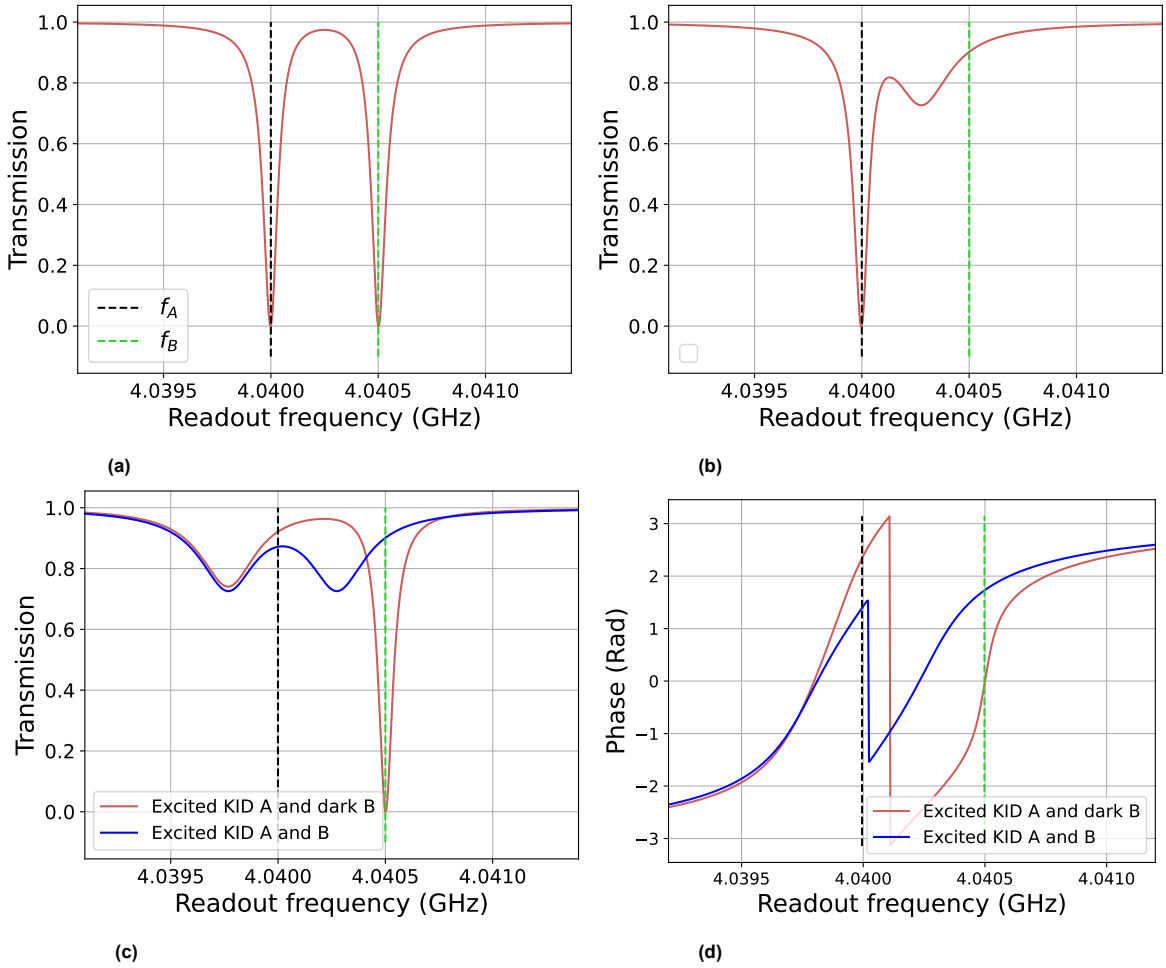

Figure 2.5: A visual explanation to understand the definition of crosstalk due to frequency collisions. Top left shows transmission dips of 2 dark KIDs 'A' and 'B' who are close frequency neighbours. Their resonance frequencies are indicated on all graphs with black and green dashed lines respectively. Top right shows the same two KIDs but now KID B has been excited by a photon. Note how the shape of KID A's dark dip changes as KID B shows a response. Bottom left shows a red line representing both KIDs at maximum response and a blue line representing the response of KID A while KID B did not get excited. Crosstalk on KID A is defined as the normalised difference between the measured phase at $\mathrm{f_A}$ after an excitation with a dark neighbour and an excited neighbour, as seen in the bottom left. Also note how phase crosses 0 exactly at the transmission minima

Phase diagrams of multiple KIDS have a sharp jump between the two resonance frequencies. To understand why this happens the overlapping resonance circles of two KIDs A and B are given in figure 2.6 where in (a) only KID A is excited and in (b) both KIDs are excited. Remembering how phase

was defined in figure 2.2 (b) between 0 and $2\,\pi$ and seeing how these circles loop around to cross the $\mathrm{im}(\mathrm{S}_{21})$ = 0 line from the positive to negative values. At that point the phase in image (a) the phase switches from +π to -π radians, creating the sudden jump in phase diagrams.

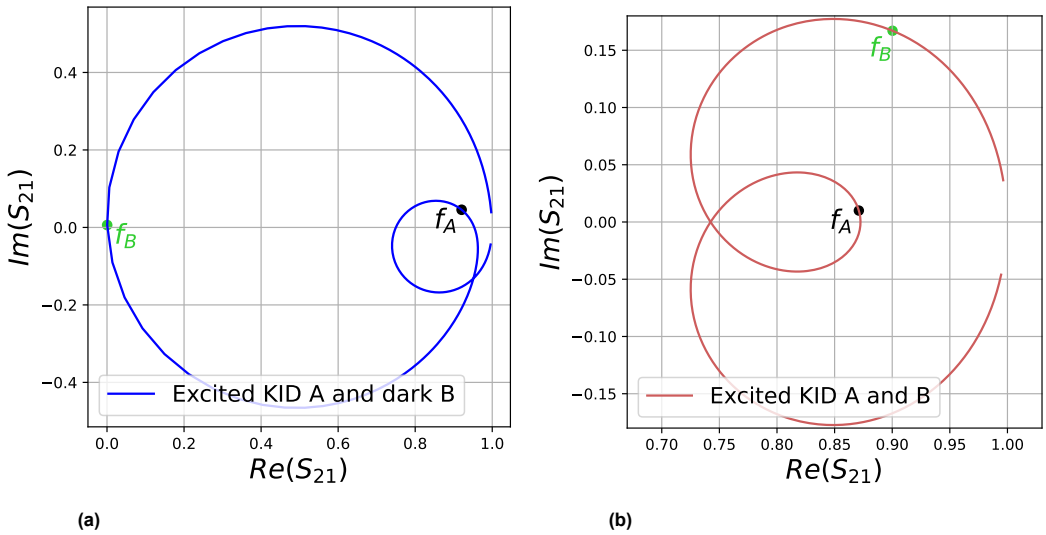

Figure 2.6: Left image showing the combined resonance circles of KID A and B where only KID A is excited. The position of both resonance frequencies are indicated. Right image showing the combined resonance circles of KID A and B where both are excited by a photon. Just after $\mathrm{f_A}$ the circle passes from the positive to negative y-axis, causing the phase jump in figure 2.5 (d).

The magnitude of frequency collisions is dependent on the energy of each incoming photon, meaning readout equipment cannot be calibrated to compensate for the change in phase. The only way to reduce collisions is to increase the frequency distance between KIDs as much as possible. Obviously all KIDs except the ones one the very edges of the bandwidth have frequency neighbours on both sides. However, since an excitation always moves transmission dips to the left (or towards its lower frequency neighbour), the state of a KID's right side neighbour will have much more of an effect. For the rest of the chapter we will only concern ourselves with collisions caused by one right side neighbour.

The magnitude of collisions is expressed through the relative changes in phase readout ϕ at resonance and will be referred to as the level of crosstalk χ_{RL}^{col} the right KID imposes the left KID through equation 2.11. Though usually we express the crosstalk in dB since the modelled crosstalk that will be discussed spans different orders of magnitude as can be seen in figure 2.7

$$\chi_{RL}^{col} = \frac{\phi_L^{R,dark} - \phi_L^{R,exc}}{\phi_L^{R,dark}} \tag{2.11}$$

Where $\phi_L^{R,dark}$ and $\phi_L^{R,exc}$ are the phases of a maximally excited left KID at its resonance frequency with a dark and excited right side neighbour respectively. Simulations are now run on KIDs with different initial frequency spacing $\mathrm{df_0}$ which are all excited by a blue $2.9\,\mathrm{eV}$ photon to get maximum response and frequency shift.

The level of crosstalk is calculated each time for different frequency spacings according to equation 2.11. The resulting graph in figure 2.7 gives the minimal distance required for any desired crosstalk level, for KIDs with quality factor Q = 5.0×10^4. The criterion was set on a crosstalk level of -$10\,\mathrm{dB}$ so we read the graph and see a minimal frequency spacing of $11.6\,\mathrm{FWHM's}$, or linewidths between all KIDs is required. Figure 2.7 also shows absolute frequency spacings for KIDs with Q = 5.0×10^4 with resonance frequencies near $4\,\mathrm{GHz}$. In absolute frequency we read a minimal spacing of $0.94\,\mathrm{MHz}$. Since the goal is to have 1000 separate KIDs on a bandwidth of $4\text{-}8\,\mathrm{GHz}$ we can at best achieve a distance of 4 MHz between KIDs if they were perfectly spaced. This gives a minimal crosstalk effect which will always be present. In this case we can not achieve less than -$33.6\,\mathrm{dB}$ crosstalk.

Note that figure 2.7 represents a worst-case scenario of crosstalk and these values are only representative of the situation where both KID A and B in figure 2.5 are excited by a blue photon. Calculating crosstalk in this way gives the most stringent yield criteria and a KID will only be considered useable if the maximum level of crosstalk caused by frequency collisions cannot exceed -$10\,\mathrm{dB}$. How often these levels of crosstalk actually occur during imaging using KIDs is entirely dependant on the use case, and the intensity of the object that is being imaged. Because the arrays were designed with a constant Q-factor, the dips at the highest frequencies will be roughly twice as wide as at the low frequency end. As a result the level of crosstalk at higher frequencies will be higher in the order of $1\,\mathrm{dB}$ if we plot figure 2.7 in absolute frequency. Looking at spacing expressed in linewidths gives more consistent results over the whole bandwidth. Crosstalk at the high frequency end is in the order of $0.1\,\mathrm{dB}$ higher when expressed in linewidths than shown in figure 2.7. Lastly, figure 2.7 assumes a constant Q-factor for all KIDs. Wider or narrower dips will have a slightly different effect on the measured phase, and as will be seen later, Q-scatter can be significant in real arrays.

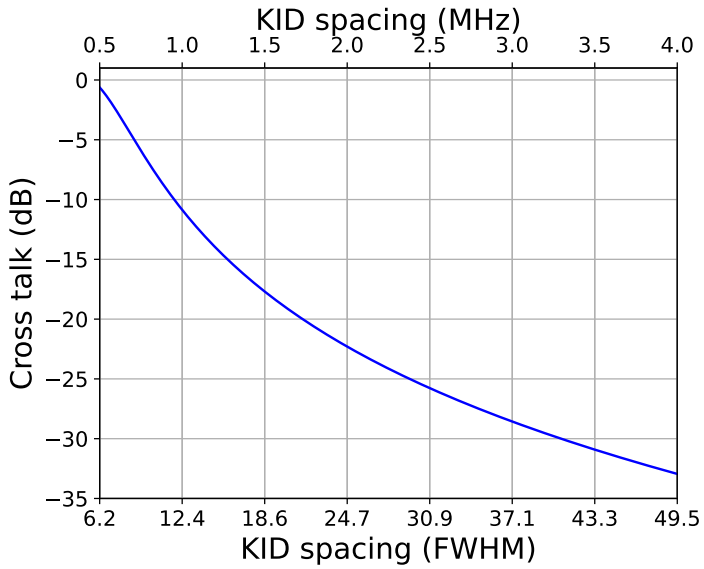

Figure 2.7: Graph showing the results of simulations using the response model to calculate crosstalk due to frequency collisions between two maximum response KIDs with Q = 5.0×10^4 as a function of frequency spacing expressed as a number of line widths and as an absolute frequency spacing for KIDs with a resonance frequency near $4\,\mathrm{GHz}$

Note how figure 2.7 does not start at $\mathrm{df_0}$ = $0\,\mathrm{MHz}$ but at $0.5\,\mathrm{MHz}$. At lower spacings the graph makes large and sudden jumps which are distracting and do not provide much useful information. Why these jumps occur can become clear from figure 2.5 (d) where the phase diagram of two excited KIDs, initially $0.5\,\mathrm{MHz}$ apart, has a large jump directly to the right of $\mathrm{f_A}$. This is a consequence of the phase in the response circle being defined a clockwise angle between -π and +π. We see that if the KIDs were placed even closer together that jump would cross over $\mathrm{f_A}$ and the result of equation equation 2.11 would be drastically different.

2.3. Smith coordinate transformations

In most cases KID response is expressed in terms of phase change at the dark resonance frequency of a transmission curve [7]. However, this response saturates for high energy photons and using a different coordinate system can help analysing response over the whole range of photon energies [19]. To this end we transform the complex transmission coefficient $\mathrm{S_{21}}$ received from the VNA into a complex value in smith coordinates Z.

$$\Gamma = \frac{\mathfrak{re}(S21) - x_c + i \cdot \mathfrak{im}(S21)}{r} \tag{2.12}$$

$$Z = \frac{1+\Gamma}{1-\Gamma} \tag{2.13}$$

where $\mathrm{x_c}$ is the x-coordinate of the centre of a resonance circle and r is the radius of that circle. The used smith coordinates then follow by taking $R = \mathfrak{re}(Z)$ and $X = \mathfrak{im}(Z)$ meaning the real and imaginary components of Z. The X smith coordinate is then analogous to phase in previously used polar coordinates. The response of a KID without any neighbours measured at $\mathrm{f_0}$ as expressed in both coordinate systems is seen in figure 2.8.

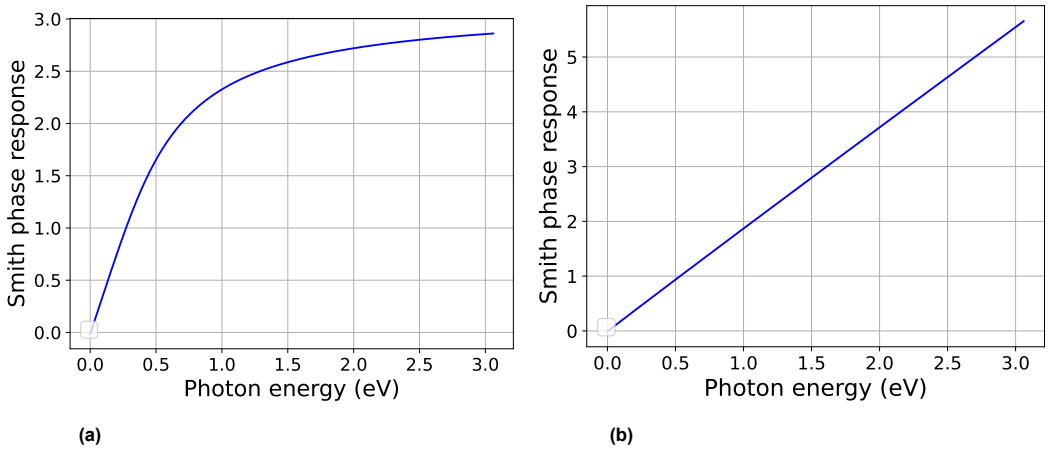

Figure 2.8: Left image showing the phase response of an isolated KID measured at its resonance frequency as a function of energy of an absorbed photon. The response shows saturation at higher energies. Left image showing the response of the same KID expressed in Smith coordinates with a linear relation to photon energy over the full range.

Because of the saturation in response seen in figure 2.8 (a), photons of higher energy will be harder to distinguish. This negatively affects the resolving power R of a KID. In figure 2.8 (b) on the other hand has, a linear response over the whole range of photon energies. To be clear, crosstalk calculated in figure 2.7 was calculated with phases expressed in smith coordinates. Further analysis done on resonance dips and cross talk due to frequency collisions will also be performed using these Smith coordinates.

2.4. Determining yield criteria

There is a limit to the number of KIDs that can be placed on a certain bandwidth. As more KIDs are placed on an array their transmission dips inevitably get closer together and crosstalk due to frequency collisions will become worse. This inherent crosstalk means there is a theoretical maximum of usable KIDs on an array. Besides that there is an issue with frequency scatter, as was seen in figure 1.4 causing some KIDs to be much closer in frequency space than designed. This effect means a practical limit on the amount of usable KIDs will be encountered before the theoretical limit is reached.

The crosstalk curve in figure 2.7 is used to define a minimal frequency distance $\mathrm{df_0}$. Earlier a tolerable crosstalk of -$10\,\mathrm{dB}$ was defined and a concurrent $\mathrm{df_0}$ of $0.94\,\mathrm{MHz}$ is calculated for KIDs with $\mathrm{Q} = 5.0 \times 10^4$. It is assumed frequency scatter will change the $\mathrm{f_0}$ of KIDs according to a normal distribution centred around the designed resonance frequency $\mathrm{f_0}$. To this end Monte Carlo simulations are run. Starting with a 4-$8\,\mathrm{GHz}$ bandwidth array with a certain number of KIDs perfectly spaced with the highest $\mathrm{df_0}$ possible, the $\mathrm{f_0}$s are randomly varied around their designed $\mathrm{f_0}$ with a certain standard deviation $\sigma_{\mathrm{\delta f/f}}$. After each simulation the percentage of KIDs that still satisfy the frequency spacing condition is checked. This percentage is referred to as the yield of the array. The result of simulations with three $\sigma_{\mathrm{\delta f/f}}$'s are shown in figure 2.9 (a). The average yield of an array over 20 simulations is plotted against the total number of KIDs on that array.

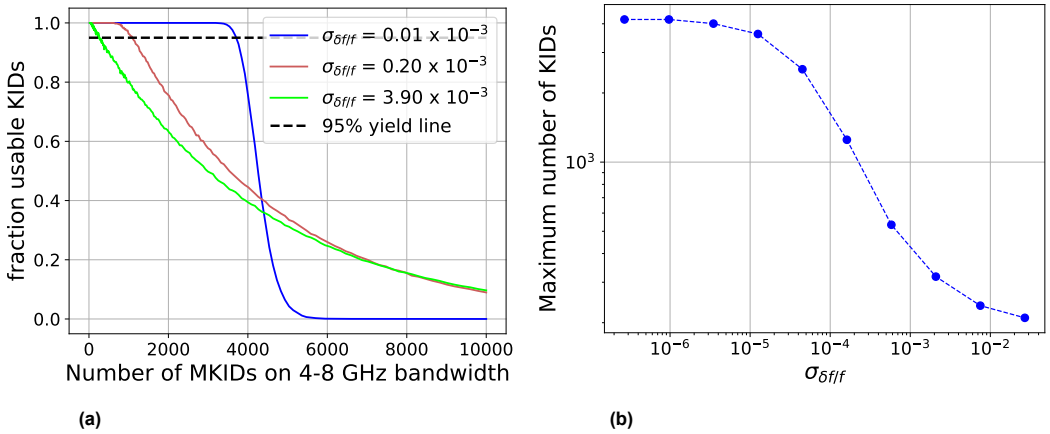

Figure 2.9: Left graph showing the fraction of KIDs that are expected to have <-$10\,\mathrm{dB}$ cross talk in an array with a certain number of KIDs with a uniform Q = 5.0×10^4, on the same $4-8\,\mathrm{GHz}$ bandwidth for three different $\sigma_{\delta \mathrm{f/f}}$. A desired yield of 95% is indicated by the dotted black line. The measured $\sigma_{\delta \mathrm{f/f}}$ from a real array is given in green, red shows the desired $\sigma_{\delta \mathrm{f/f}}$ and blue shows an extremely low $\sigma_{\delta \mathrm{f/f}}$ nearing the absolute limit. Right graph showing the maximum achievable number of KIDs with <-$10\,\mathrm{dB}$ cross talk at 95% yield on a $4-8\,\mathrm{GHz}$ array for some $\sigma_{\delta \mathrm{f/f}}$.

Clearly a lower $\sigma_{\delta \mathrm{f/f}}$ allows for larger arrays. We demand an expected $95\,\%$ of KIDs on the array should satisfy the frequency spacing condition. Figure 2.9 (b) then shows a graph where the maximum number of KIDs on an array with a 4-$8\,\mathrm{GHz}$ bandwidth, with a yield of at least $95\,\%$ is plotted against the scatter $\sigma_{\delta \mathrm{f/f}}$. For each point in figure 2.9 (b) one line like the ones in figure 2.9 (a) is made. We then find the intersection between that graph and the 95% yield line. The important result of all these calculations is that a requirement on scatter can now be set for an array of any desired size. For this work specifically it will be noted that a maximum scatter of $\sigma_{\delta \mathrm{f/f}}$=$0.2 \times 10^{-3}$ can be allowed to be able to reliably create a 1000 pixel array.

2.5. Electromagnetic cross talk

EM cross talk has not been modelled or experimentally ruled out in this thesis. Literature suggests that, as long as the array has no frequency neighbour KIDs spatially next to one another, the addition of EM cross talk to scatter should be minimal [20]. Additionally, EM cross talk has a characteristic effect on the transmission dips of the affected KIDs, where avoided crossings of resonance frequencies cause one dip to deepen and broaden extremely while the other becomes shallow [21]. This effect was clearly observed in earlier arrays that experimented with having KIDs on a common ground. Arrays analysed in this work all have floating ground KIDs and did not show such deformations. Furthermore, as will be seen in section 4.4 an array design has been used that ensures KIDs close together in frequency space will be far apart on the array.

3

Fabrication and Post-Processing

Now that design requirements on arrays have been determined, a close look is taken at some possible sources of frequency scatter, beginning in this chapter with tolerances in the fabrication process of KID arrays. A change or uncertainty in the dimensions of the IDC and inductor will vary the capacitance and inductance of a KID respectively. It is important to understand how KIDs are fabricated as a very similar process will be used in chapter 4 for an IDC trimming experiment.

3.1. Lithographic array fabrication

KID arrays are fabricated in a very similar manner to regular semiconductor electronics at micron scale or smaller. The needed materials are deposited on a (in this case) sapphire $100\,\mathrm{mm}$ diameter, $350\,\mu\mathrm{m}$ thick wafer and parts of the material is removed by a lithographic process, leaving behind only the intended structures. A slightly different procedure is used for subsets of components in the array. The general process of array production is visually described in figure 3.1.

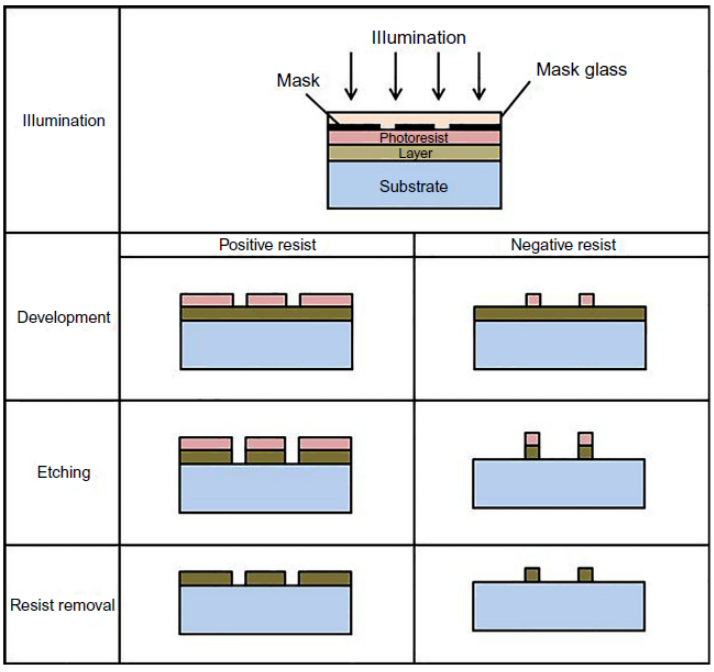

Figure 3.1: [22] A visual description of the general process of optical lithographic chip fabrication. A distinction is made for the use of positive and negative resist. A very similar process is used for EBPG except that there is no mask required. the E-beam is projected directly on a wafer, using pre-patterned markers for alignment.

Before delving into the slight differences in production the general technique for all components is described. First a layer of either NbTiN or $\beta - \mathrm{Ta}$ is deposited on the whole substrate, which is the sapphire wafer. Then photoresist is spun on top of the metal layer to also cover the whole wafer. Highly localised chemical reactions will take place in photoresist when it is illuminated to which will change the solubility of the resist. A mask is fabricated according to our design of the array so only the correct parts of the wafer will be illuminated. Next comes the development stage where the soluble portions of the resist are dissolved and removed, exposing metal to be etched away. Here reactive ion etching is applied to remove undesired material. Sulfur hexafluoride ($\mathrm{SF6}$) is used, which reacts with exposed metal. Finally, the non-illuminated resist is removed and the wafer is cleaned. We are then left with the sapphire substrate and a clearly defined structure of the array.

Before array fabrication is described step-by-step, two distinctions in procedures are made. Firstly we discriminate between optical lithography and electron beam pattern generation (EBPG). The difference between the two is in the Illumination stage. Optical lithography uses UV light to illuminate photoresist through a mask whereas EBPG sends a tight beam of electrons directly to the resist. Components in the array that are more sensitive to small variations in line dimensions will be written with EBPG which will take more time than optical lithography would have but will result in more accurate structures. For large components for which precise dimension are not critical, optical lithography is used. Second, each step uses either a positive or a negative photo-resist. This distinction is also made in figure 3.1 and the two react differently when exposed to UV light or electrons. Positive resist is illuminated on areas where deposited material is intended to be removed. When exposed to light the resist locally reacts and becomes more soluble. Negative resist is illuminated only on areas where material is intended to stay and becomes less soluble when exposed to UV light or electrons. After development the illuminated resist is then washed away, exposing the metal below to be etched.

The following list gives the exact used lithographic method for each subset of components in the array in the order in which they are fabricated.

1. The ground plane: a $150\,\mathrm{nm}$ thick layer of NbTiN is deposited and, using positive resist, EBPG markers and the readout-line are etched using optical lithography.
2. IDCs and coupler bars: What is left of the NbTiN from step one is used again here. Using a positive resist and a $10\,\mathrm{nm}$ step size for EBPG, the metal is etched to leave behind all IDCs and coupler bars.
3. Coupler and ground plane bridges base: These will be physically placed over the readout line so first a $600\,\mathrm{nm}$ thick layer of polyimide is deposited and 'softbaked'. Optical lithography is used and the base for the bridges are etched.
4. Inductor and bridges: $47\,\mathrm{nm}$ thick $\beta - \mathrm{Ta}$ is deposited, negative resist is spun and all inductors, coupler bridges and ground plane bridges are etched out. The finished array is cleaned using High energy oxygen ions that form a plasma.

Later in chapter 4 arrays fabricated with the process described above will be subjected to another round of EBPG to trim some IDCs to adjust the f_0 of scattered KIDs. For this post-processing no new layer of NbTiN needs to be applied since already existing IDC fingers will only be shortened. For trimming a negative resist and a $10\,\mathrm{nm}$ step size EBPG is applied.

3.2. Fabrication tolerances

In chapter 2 the EM effects in the array were assumed to contribute insignificantly to frequency scatter. The second cause of f-scatter that was considered are physical imperfections in KIDs caused by the fabrication process. A mismatch in designed and produced line width and length of the capacitor, inductor and coupler bar will cause scatter as it causes a change capacitance and inductance, shifting the resonance frequency through equation 2.10. Tolerances in the fabrication of KIDs are measured with Scanning Electron Microscope (SEM) images. An edge detection algorithm is made to determine exact dimensions of specifically IDC fingers of several KIDs. Analysis on inductor lines was also attempted but did not yield useful results because, as can be seen in figure 3.2, there is low contrast between the $\beta - \mathrm{Ta}$ inductor and the sapphire wafer. This made edges of inductor lines less clearly defined and makes edge detection difficult to achieve.

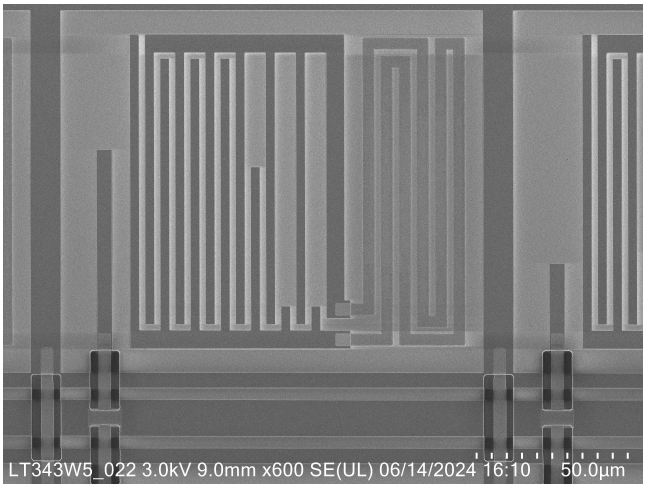

Figure 3.2: SEM image of a KID and part of the troughline with bridges in the 400 pixel LT343 array

3.2.1. SEM image edge detection

To determine the tolerances in line widths and lengths with nanometer precision close up SEM images of only IDC fingers are made. Each pixel in a SEM image represents known dimensions on the chip. Figure 3.3 (a) shows one such image. The wider dark strips are NbTiN fingers and the narrow light strips are gaps so we see the sapphire wafer. To make determining line thickness easier Fourier filtering is used to remove some noise present in the images. We first apply a 2D Fourier transform to a close up image of an IDC to get frequency information. The noise in SEM images is represented by lower frequencies than the hard edges of IDC fingers we are interested in, so a mask is applied to the data in Fourier space to remove lower frequencies from the image and create a high-pass frequency filter. For the purposes of this analysis a simple circular mask in the centre of the Fourier transformed image is sufficient. The filtered frequency data is then transformed back to create an image as can be seen in figure 3.3 (b). Note how there is no longer a contrast between the sapphire wafer and NbTiN but there are well defined bright lines on the edges of the IDC fingers.

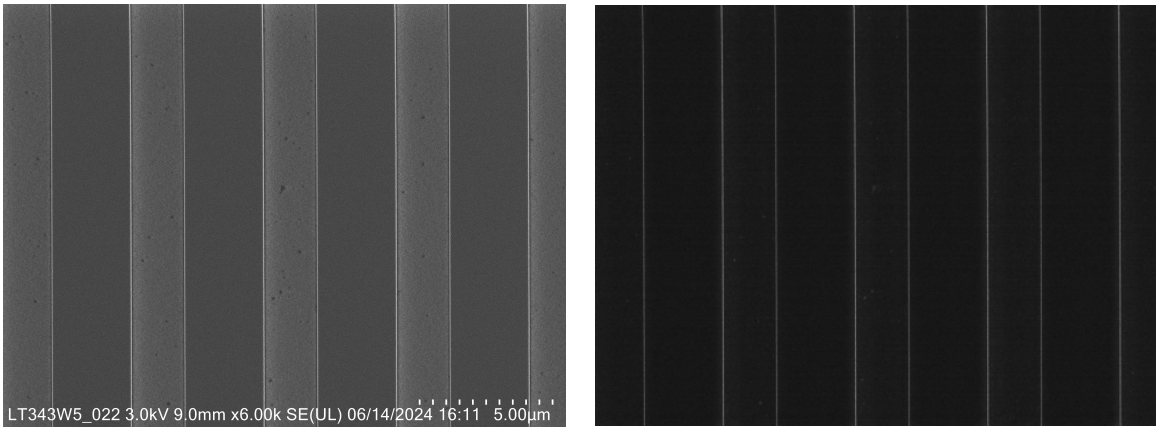

(a) **(b)**

Figure 3.3: Left image showing a SEM image of an IDC of one KID on the grounded 400 pixel LT343 array. Right image showing the same IDC after high pass Fourier filter.

Now widths of both the IDC fingers and the gaps between them can be determined for every line of pixels in an image. Every pixel of these filtered images has a value representing the 'brightness' of that pixel. The edges of the IDC fingers then look like peaks in each line of data. Peak finding functions in python are used to determine the location of these peaks in every row of pixels in an image separately. Every row should be evaluated separately because that way the KID can be slightly rotated between

images and the measured widths would stay the same. Since the physical width of one pixel on the IDC is known, the width of the IDC fingers is calculated by counting the number of pixels between two peaks. To ensure an edge detection will be equally effective over all data and for every images each row of the filtered images are normalised separately so settings in peak finding functions won't have to be changed for every row.

An example of the resulting distribution of found widths in an image can be seen as a histogram in figure 3.4. Note the distribution has two sharp peaks, one for the NbTiN fingers and one for the gaps between the fingers. The shape of these peaks will be used to describe fabrication tolerance within one KID. The average values of this dataset will be compared to the averages of other images to quantify the fabrication tolerance between KIDs. Interesting to note is that the IDCs were designed to have $3\,\mu\mathrm{m}$ wide fingers and $2\,\mu\mathrm{m}$ wide and gaps. We see the distributions are slightly offset. The fabricated fingers are $25\,\mathrm{nm}$ narrower than designed and as a result the gap width has increased.

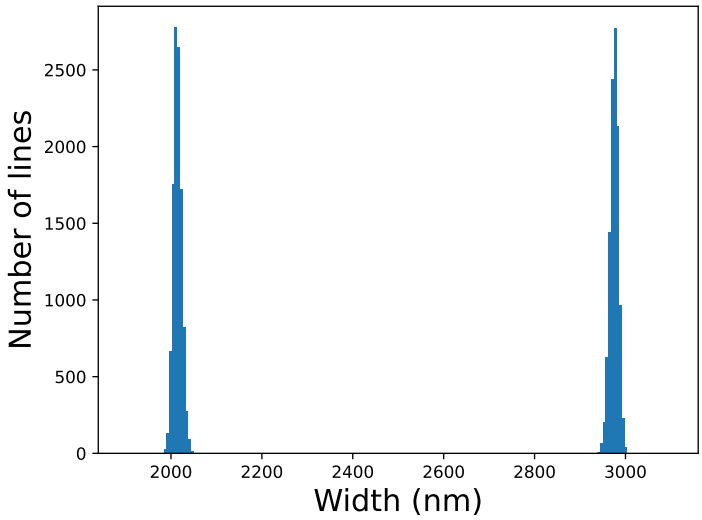

Figure 3.4: Example of histogram resulting from edge detection on an IDC image. The two peaks indicate widths of capacitor fingers and the gaps between them.

A similar approach is used to determine tolerances on the finger lengths. However to be able to fairly compare different IDCs only images containing 'empty' fingers are used for this analysis since they were all designed to be equally long at $80\,\mathrm{um}$. An alternative would be to compare the 'full' fingers. However to fit an entire finger on one image we would need to zoom out with the SEM, sacrificing precision in the measurement.

3.2.2. Modelling of geometric defects

Once the production tolerances in the KIDs are known, line geometry needs to be related to inductance and capacitance. To this end an analytical model of a simplified IDC is used [23], where a certain number of fingers are fully filled and total finger length is adjusted by increasing or decreasing the length of all fingers equally. Capacitance C of and IDC in this model is then calculated by:

$$C = (N-3)\frac{C_I}{2} + 2\frac{C_I C_E}{C_I + C_E} \tag{3.1}$$

Where L is the length of one finger, N is the total number of fingers in the IDC, $\mathrm{C_E}$ is the capacitance between an external finger, and the ground plane an $\mathrm{C_I}$ is half the capacitance of one internal. Both of these capacitance terms are calculated with semi-infinite layer approximations [23], dependant on finger width and length.

$$C_I = \epsilon_0 \epsilon_r L \frac{K(k_I(W))}{K(k'_I(W))} \tag{3.2}$$

$$C_E = \epsilon_0 \epsilon_r L \frac{K(k_E(W))}{K(k'_E(W))} \tag{3.3}$$

Where ϵ are permittivities, K are elliptical integrals with modulus $\mathrm{k(W)}$, dependant on finger width W and $\mathrm{k'} = \sqrt{1-\mathrm{k}^2}$. Comparing values for C with from this model and SONNET with the same total finger length shows poor agreement. This model can be used to estimate a shift in resonance frequency due to small changes in line geometry sufficient accuracy, but not to calculate the absolute capacitance or resonance frequency of any KID.

Figure 3.5 shows the resulting graphs of how resonance frequencies change with line dimensions [24]. The black dashed lines show one standard deviation of width and length in figure 3.5 (a) and (b) respectively. From the same graph these tolerances can then be translated to frequency scatter, indicated by the red lines in both graphs. These simulations are done on the high end of the readout bandwidth as this is where KIDs are most sensitive to variations finger dimensions and we are again interested in a worse-case scenario to determine the effects of fabrication tolerances.

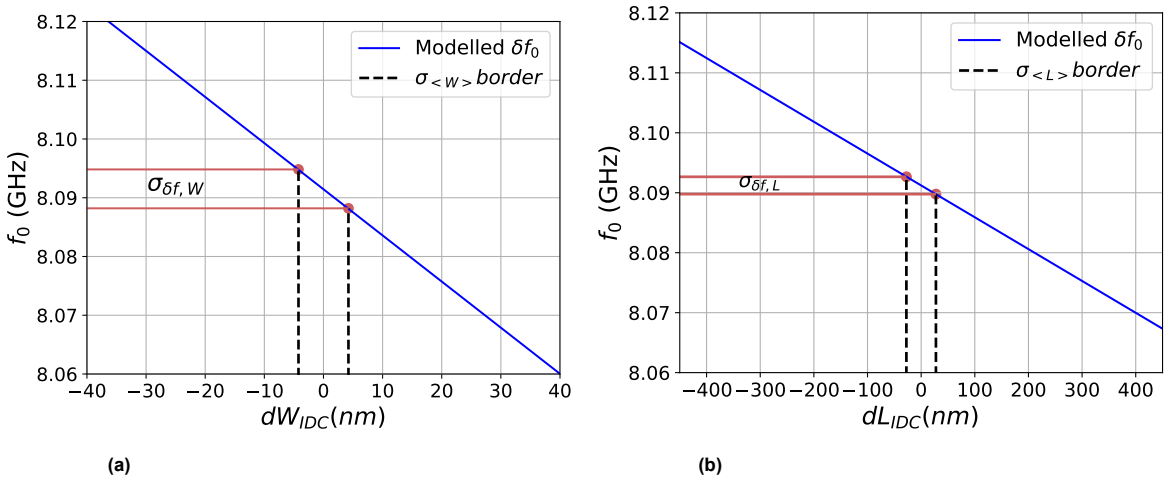

Figure 3.5: [24] Left shows how deviations in IDC finger width is modelled to affect the resonance frequency of a KID. The dashed black lines indicate a certain standard deviation in line width. The red lines show how tolerance in line width is translated to a frequency scatter. Right shows dashed black lines for the standard deviation in total IDC finger length. Again the red lines show how fabrication tolerance is translated into frequency scatter.

From figure 3.5 it can be concluded that KIDs are much more sensitive to changes in finger width than they are to changes in finger length. It is partly for this reason that we will choose to trim IDC fingers in their length instead of their width during post processing since the length method will be more forgiving in terms of misalignment and will allow us to adjust the whole array more accurately. The two f-scatter values are used to calculate a total scatter caused by variations in IDC line dimensions through error propagation theory:

$$\sigma_{\delta f/f,IDC} = \sqrt{\sigma^2_{\delta f/f,W} + \sigma^2_{\delta f/f,L}} \tag{3.4}$$

Where $\sigma_{\mathrm{\delta f/f,W}}$ and $\sigma_{\mathrm{\delta f/f,L}}$ are frequency scatter caused by tolerances in width and length respectively. $\sigma_{\mathrm{\delta f/f,IDC}}$ is the total f-scatter caused by fabrication tolerances in the IDC.

4

Methodology

4.1. KID readout

Superconducting detectors requires different readout equipment than semiconductor or CCD devices where photons excite electrons creating a response in the form of a measurable current. $\beta - \mathrm{Ta}$ needs to be cooled to below $1\,\mathrm{K}$ to become superconductive [19] so the array is embedded in a Bluefors cryostat. The schematic also shows the three temperature stages of the cryostat and readout electronics being progressively cooled further until the $0.1\,\mathrm{K}$ stage is reached. A detailed CAD image of the cryostat is given in figure 4.1 (a).

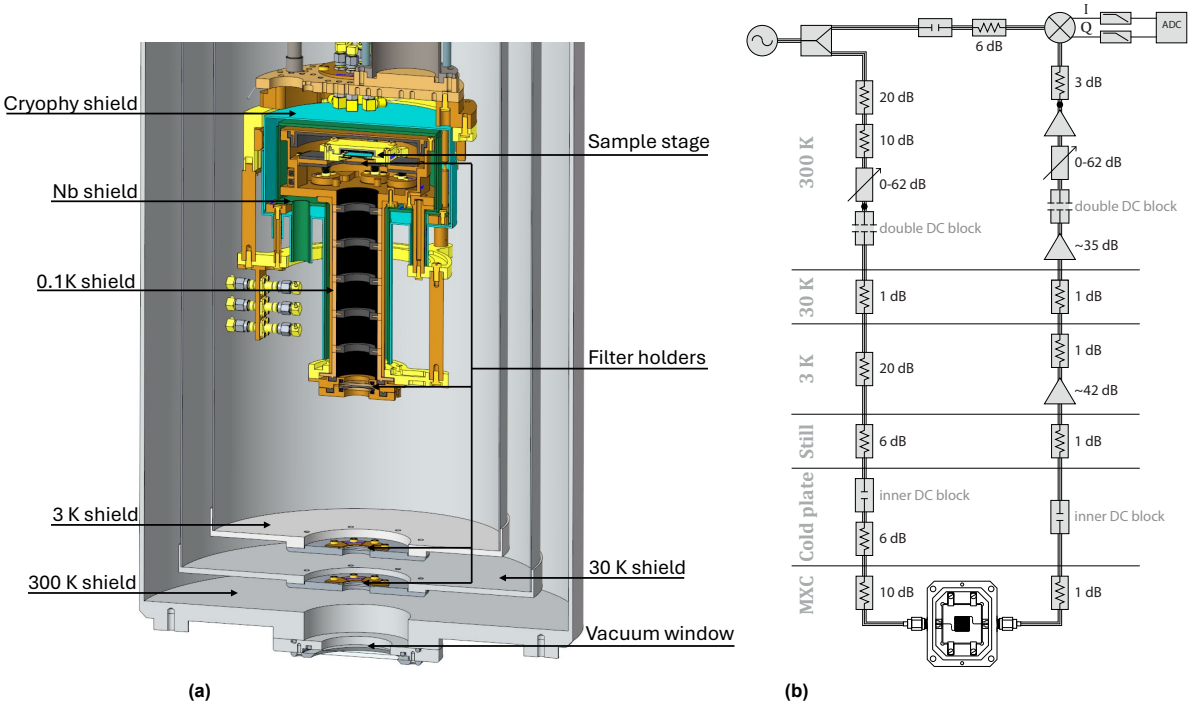

Figure 4.1: Left A CAD model of the cryostat used to perform cool down KIDs below $\mathrm{T_c}$. Arrays are placed in the sample stage and are magnetically shielded by a layer of cryophy and a layer of Nb. If needed, light can enter the cryostat through the vacuum window for response measurements.(b) [25] A schematic of the used readout equipment for KIDs in several layers of a cryostat. An incoming signal is first attenuated twice at different temperature stages before being passed through a KID array. As the signal exits the cryostat it then gets amplified at different temperature stages before being read out in the VNA.

To measure response of a KID device, a signal current containing all f_0's in the array is sent through the device and the transmission of that signal is measured using a VNA. A schematic drawing of the measurement setup is shown in figure 4.1 (b). Note how the signal is attenuated at every stage to reduce thermal noise. After passing through the array the signal is amplified again at the 3 and $300\,\mathrm{K}$ stages so the VNA can do accurate measurements.

4.2. Q-factor analysis

Without knowing to what KID in the array every transmission dip belongs to, an analysis can already be done for quality factors Q in the fabricated array. We are especially interested in the coupling quality factor Q_c since this value can be tweaked more easily in future designs. Also the overall Q should be limited by coupling. To this end separate dark VNA scans with high frequency resolution are run around every dip. An example of one such scan is seen in figure 4.2. The Q of a transmission dip can usually not be calculated simply by taking the full width half maximum because most dips will be deformed in some way. The signal power provided by the VNA plays a large role in deforming dips. Higher power scans will be less noisy but change dip shape more. Scans with powers between $-116\,\mathrm{dBm}$ and $-94\,\mathrm{dBm}$ are performed and scans at $-110\,\mathrm{dBm}$ are estimated to have the best balance between noise and deformation. Impedance mismatching and environmental effects also have an impact on dip shape.

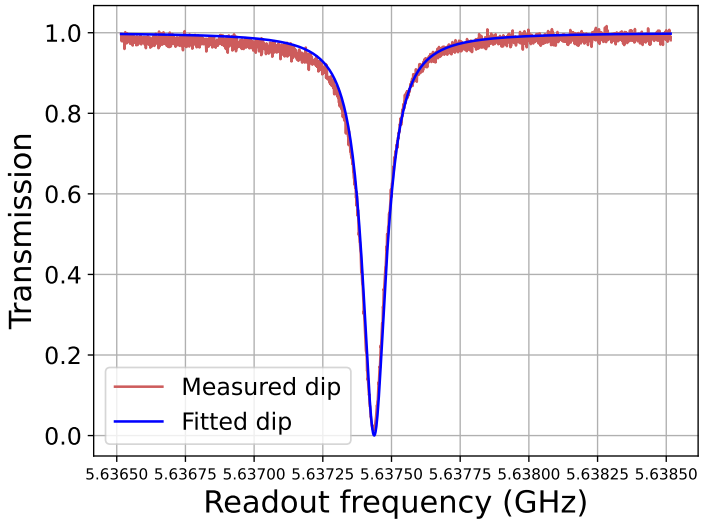

Figure 4.2: A measured transmission dip of one KID in the LT361 array together with the fit used to determine Q_c. The VNA scan was performed with a $-116\,\mathrm{dBm}$ signal power through the array.

To extract a Q_c from the scan the transmission dip is fitted using a model which makes an algebraic fit of the resonance circle [26]. One result of such a fit is given in figure 4.2 on a measurement at $-116\,\mathrm{dBm}$. The total Q is found from a minimisation of an algebraic expression on the fit and the coupling factor can be calculated using geometric relationships in the resonance circle[27].

$$Q_c = \frac{|Z_c| + r}{2r} Q \tag{4.1}$$

Where Z_c is the centre of the resonance circle in the complex plane and r is the radius of the resonance circle.

4.3. Effects of measurement setup

To ensure results gathered from measurements in the cryostat are reliable and reproducible we first check if the measurement setup itself introduces some form of scatter. Also some tricky effects like flux-trapping [28] might cause scatter and make different measurements difficult to compare. To quantify

these effects an experiment was done using a 6x6 KID array. This array is placed in the cryostat and cooled down several times and subsequently scanned using a VNA. For each scan the resonance frequency is found using the same peak finding algorithm and the difference between the found values is used to calculate scatter occurring between measurements. Four cooldown cycles were applied and their scans are shown in figure 4.3. For the first scan the array was cooled down all the way from room temperature. For cycles 2 the array was warmed to $175\,\mathrm{K}$, before cooling back down to $0.1\,\mathrm{K}$, so the KID was definitely not superconductive between measurement. For the third cycle the KID was warmed to $21.8\,\mathrm{K}$, still above the critical temperature of NbTiN ($\mathrm{T_c}$ = $15\,\mathrm{K}$). Finally the array was warmed to $26.8\,\mathrm{K}$ before cycle 4. The bottom graph in figure 4.3 shows a small section of all 4 scans with the transmission dip of one particular KID in the array. We see that there is some scatter happening between cycles and that the KIDs can move to either higher or lower frequencies after a cycle. There is an especially large shift seen for cycle 4. This is likely a VNA calibration issue and not a scatter as we defined it.

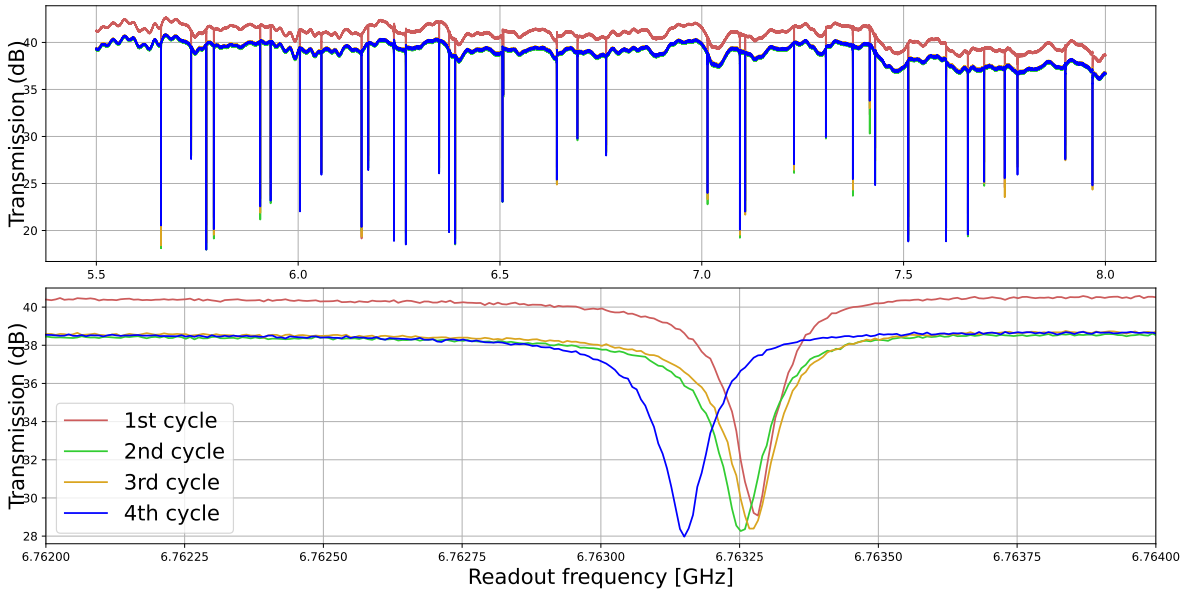

Figure 4.3: VNA scans of cooldown experiments on a 6x6 KID array. Top figure shows the full readout bandwidth with all 36 KIDs in 4 separate cooldown cycles. Bottom figure shows a small bandwidth of the same measurements focussing on a single KID. We see the KIDs experience minimal scatter across measurements.

4.4. Spatial mapping of KIDs

In order to actually determine the frequency scatter present in fabricated arrays, every KID must be matched to the correct transmission dip in the VNA scan. Mapping experiments have been performed to locate every dip in the array. To keep track of KIDs in the array they are all given an ID in order of increasing $\mathrm{f_0}$. Figure 4.4 shows a schematic representation of the designed array where every numbered square represents a KID with a corresponding ID. A few notable ideas are taken into account in the placement of $\mathrm{f_0}$'s in an array. Firstly, frequency neighbours need to be placed far enough apart such that electromagnetic cross talk can be avoided. Secondly, a smart array design can help speed up the mapping experiments and simplify data analysis. A row-wise designed of increasing $\mathrm{f_0}$ was settled on where all spatial neighbours in any given row should have 19 transmission dips between them in frequency space and each row is shifted by 7 spaces compared to the previous one. Due to f-scatter some spatial neighbours will have a few dips more or less between them but as long as the scatter in an array is comparable to that of previously mapped arrays it is extremely unlikely that two spatial neighbours will switch positions in frequency space. Why this helps with mapping experiments will be discussed in section 4.4.2.

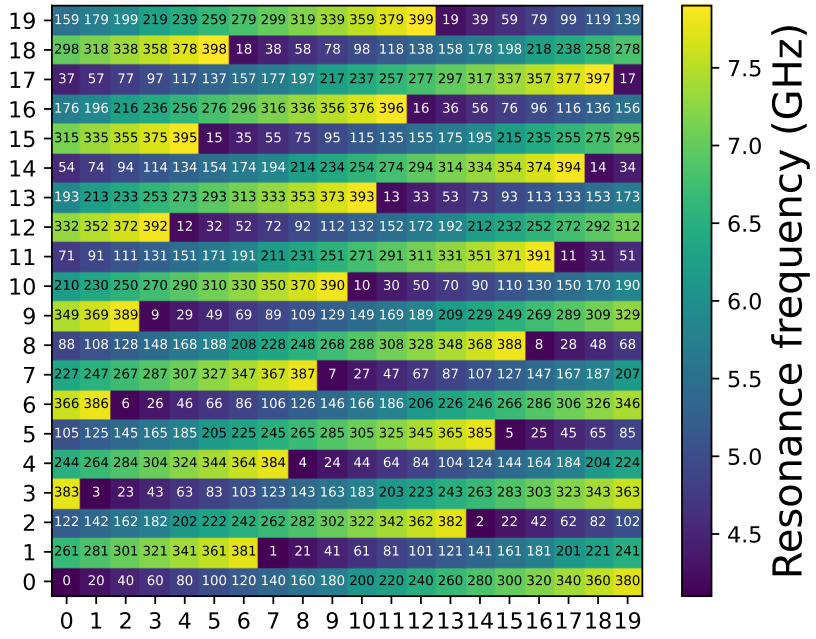

Figure 4.4: A spatial map of the designed resonance frequencies on the array of the LT361 chip. Numbers on the array indicate the ID of a KID sorted by increasing f_0. The array was designed such that the f_0's of spatial neighbours on any given row are spaced enough apart that their transmission dips are extremely unlikely to switch positions in frequency space.

4.4.1. Mapping setup

KIDs will be spatially identified by projecting a thin line of LED lights onto one row or column of the array. A VNA scan is then run which will clearly show KIDs in the illuminated line responding to the incoming photons. The light is then shifted to illuminate the next row or column of KIDs and another scan is run. Figure 4.5 shows an image made with CCD camera of light being reflected off a 400 pixel array with black lines indicating the moveable projection that will be illuminated during a VNA scan. A smartphone with OLED screen is used as a light source. The OLED screen is a requirement as some other screens will have some backlight on 'black' parts of the screen whereas OLEDs will actually turn off when the screen displays black so KIDs will not get hit by photons outside the illuminated light. Looking closely at figure 4.5 some structure can be seen in the reflected light. These are in fact lit pixels on the used smartphone. An app has been developed [29] to control the location and width of the illuminated lines during the experiment. The fact that smartphones are used introduces some variability between each experiment as some phones will have different light intensities and more importantly different pixel sizes and different layouts of pixels on their screens. However, as long as the projected line is thinner than the width of one KID the reproducibility of the experiment is not affected.

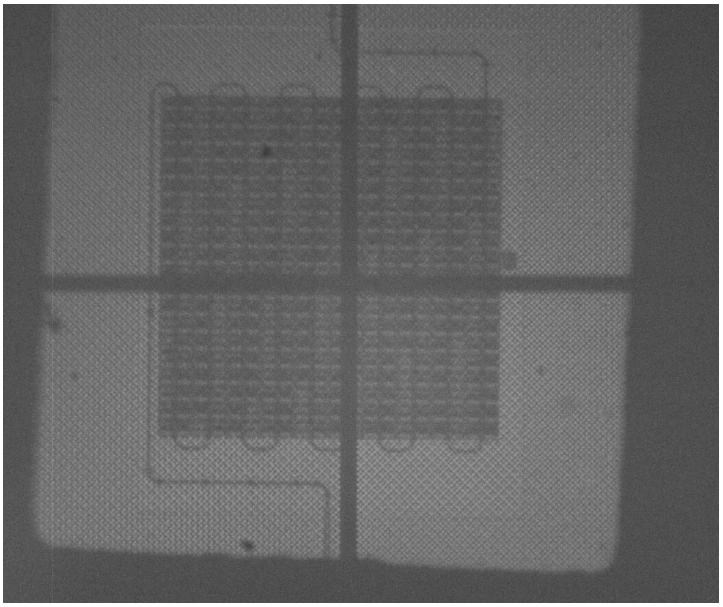

Figure 4.5: Image taken with the CCD camera in the mapping setup during optical table alignment. We see light coming from a phone screen reflected from the array, and lines which can be lit and moved across the array to perform an scan of rows or columns. These dark lines are purely illustrative, during a scanning experiment the inverse of this image is illuminated.

For effective mapping the projected lines should be in focus on the array, which will be the image plane in the optical setup used. A schematic drawing of the experiment is given in figure 4.6 showing the smartphone as a light source at the object plane, extendable lens tubes and mirrors to guide the image, a beam splitter to project the image on the array and allow the reflections to pass through to the CCD camera, and a lenses to focus the light beam. Initial estimates for needed length of the lens tubes are calculated using the thins lens equation.

$$\frac{1}{f_{lens}} = \frac{1}{x_o} + \frac{1}{x_i} \tag{4.2}$$

Where $\mathrm{f_{lens}}$ is the focal length of the lens, in this case $300\,\mathrm{mm}$, $\mathrm{x_o}$ is the distance between the lens and object plane and $\mathrm{x_i}$ is the distance between the lens and the image distance. A live feed from the CCD camera is important for aligning and focussing mapping experiments even though it is not actually used during measurements. The optical setup is built on a moveable optical table which will be positioned underneath the cryostat. First the camera is used to align the optical table such that the light reflected from the array is projected on the middle of the CCD chip. Then the camera is used again to more finely tune arm lengths in the setup to create a sharp image. Additionally figure 4.6 shows two Irises, or apertures, which can also assist in making a sharp image. Since arms at the display as well as the CCD can be extended and retracted the setup also allows for an adjustable magnification of the image. It could be necessary to adjust magnification for example if pixel sizes on the used phone are too large compared to the dimensions of a KID.

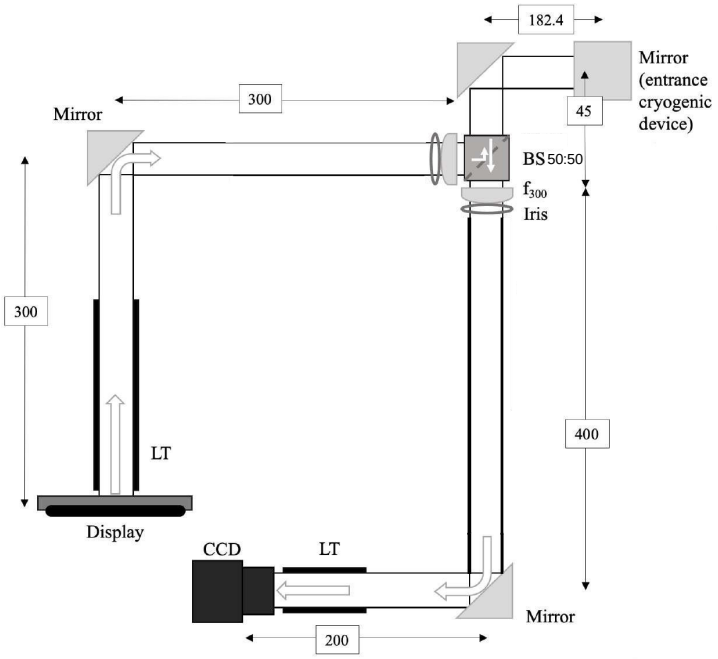

Figure 4.6: [30] Schematic drawing of the used mapping setup. Distances are expressed as maximum arm lengths in millimetres and thick black lines are used to indicate extendable lens tubes (LT). A smartphone is used as a light source placed at 'display' which projects lines on the array in the cryostat. Light reflected off the array is captured by a CCD camera which is used for alignment.

After the table has been aligned and the lens tubes fastened in position we first perform a VNA scan with a completely dark phone screen. This scan will be taken as a baseline to compare the rest of the scans to. Now the CCD camera is used again to determine the position of illuminated lines on the array. Every VNA scan requires one whole row or column of KIDs to be excited so after each scan the line seen in figure 4.5 is moved to cover the next position in the array until all kids have been hit.

4.4.2. Mapping data analysis

The result of mapping experiments are 20 VNA scans, each with a different row of KIDs illuminated, and one dark scan taken as a baseline to compare all other scans to. An illuminated KID will absorb photons from the display and its dip will show a clear response in the VNA scan. An example of one transmission dip changing over different scans is seen in figure 4.7 (a). The depth of the transmission dip of every KID is measured at the f_0's of the dark scan, resulting in a plot like figure 4.7 (b) for every KID. We know the transmission increases as a KID absorbs a photon so the change in dip depth will be a positive value. In the resulting graphs we should see a very clear peak in the data, in this case a KID with its f_0 at $6.3092\,\mathrm{GHz}$ shows strong response at scan position 3. The scan positions correspond with the line of light being projected over the row of KIDs in figure 4.4 with the same number. In this example it can be concluded this KID is positioned somewhere on the fourth row of the array. In a perfect experiment one would find 20 of such peaks for every scan position representing the 20 KIDs in each row.

Now we have 20 groups of transmission dips each belonging to a row in the array, giving a y-coordinate on the array of the corresponding KIDs. The array design used here now greatly simplifies the process of matching each dip to a specific KID in these rows, providing the x-coordinates. Since all dips in a row are all spaced sufficiently spaced far enough apart in frequency space that switching their f_0's is near impossible, the KIDs in a row can simply be ordered by increasing f_0 and given a x-coordinate. The ordering is then shifted by 7 positions and wrapped back around to fit the array for each row as was designed in figure 4.4.

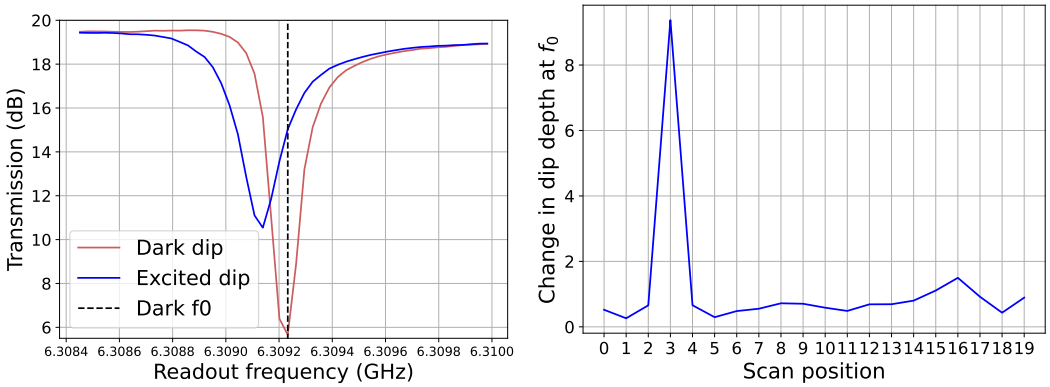

Figure 4.7: Mapping experiment results for a single KID in the LT361 array. Left figure showing transmission dips of that KID during a dark measurement with a red curve and during a scanning measurement where this KID is excited with a blue curve. Right figure showing the change in transmission at resonance as compared to the dark measurement, transmission increases after an excitation so the change is positive.

Note that this method only works for arrays with a row-wise design like in figure 4.4. In previous designs, the resonance frequencies were differently spread so it was possible for KIDs in the same row to flip positions in frequency space. For these arrays scans with illuminated columns and rows are both necessary to definitively map a transmission dip to a spatial position in the array. After mapping ID's are given to each KID by ordering the measured resonance frequencies instead of the designed valued that are given in figure 4.4. The ordering in each row has remained the same however.

4.5. Capacitor trimming

Suppose a large array of KIDs is fabricated with a certain amount of f-scatter that leads to a decrease in pixel yield. Several post-processing techniques have been suggested to improve frequency spacing [31] [11] after fabrication. One advantage of IDC trimming specifically is that even without identifying exact sources of scatter in an array, pixel yield can be improved. A technique for etching away IDC fingers has been developed and broadly consists of four steps. First an array of KIDs and their resonance frequencies need to be spatially mapped as described in 4.4. Secondly an algorithm is applied which determines what KIDs don't conform to the previously defined design requirements calculates by how much they should be moved in the frequency domain. That information is used to calculate the trim lengths dL that will be removed from the IDC fingers. Thirdly we split the KIDs in three groups: one control group which is not trimmed at all. This group is there to observe any effect the EBPG process has on the array. Then we have two experimental groups, the first is the 'offset' group, which first trimmed only by $80\,\mathrm{nm}$ to account for misalignment of the E-beam. The second experimental 'variable' group is also trimmed by $80\,\mathrm{nm}$ in addition to another variable length calculated with a trimming algorithm. An E-beam pattern is designed to trim IDC fingers of each KID as calculated, this can be done with up to $10\,\mathrm{nm}$ precision. Lastly the trimmed array is spatially mapped again to determine if all KIDs changed their resonance frequencies as expected. Figure 4.8 shows how the trimming algorithm is applied on a real array.

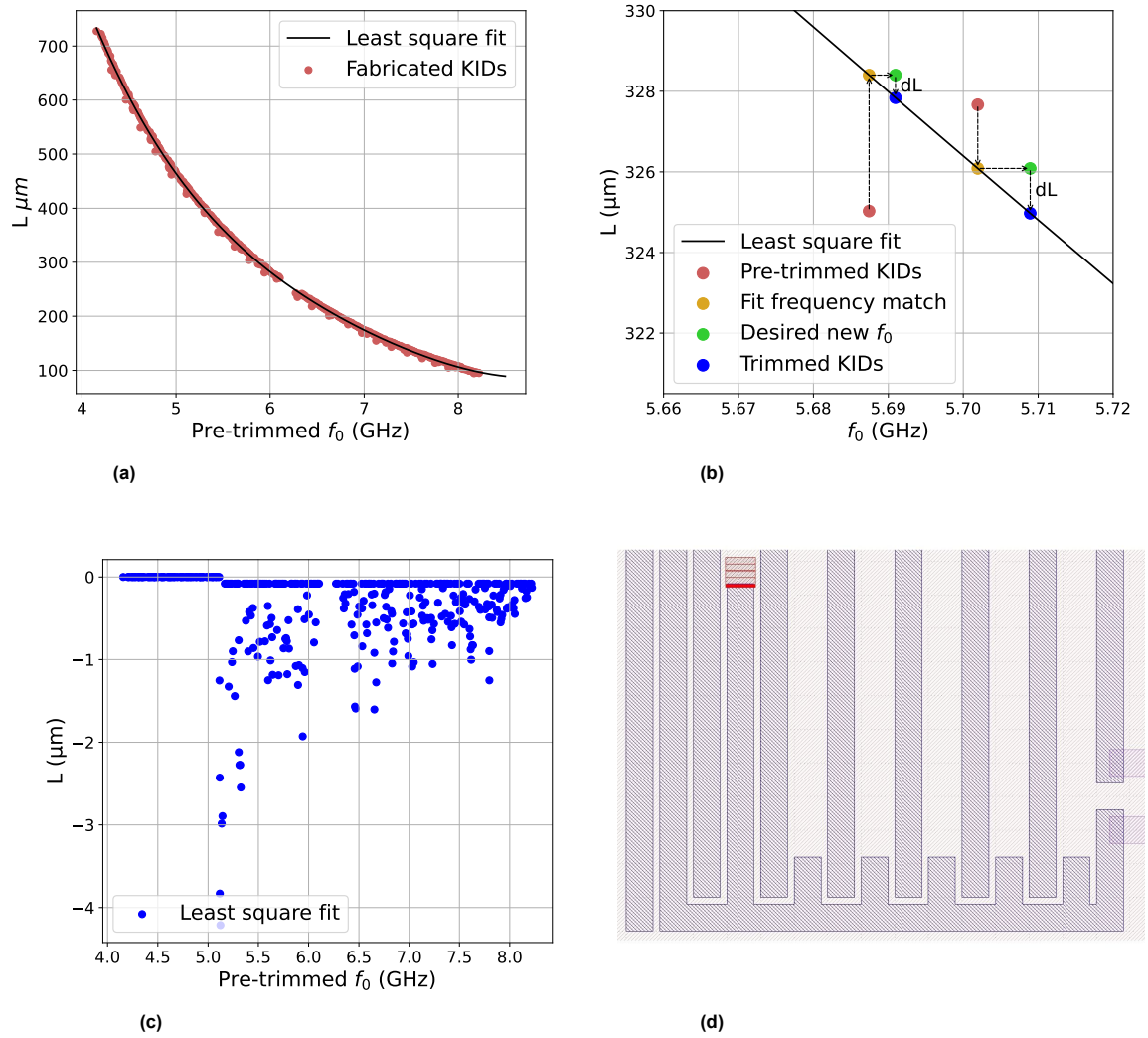

Figure 4.8: A visual explanation to understand the trimming algorithm. Top left shows the designed total IDC finger length plotted against the measured $\mathrm{f_0}$ before trimming. The black line indicates a least square fit on this data. Top right shows a small segment of the top left graph highlighting 2 KIDs (red) in the array. The arrows show how both KIDs are matched with the point on our fit (yellow) with the same frequency. We also see the desired $\mathrm{f_0}$ resulting from the algorithm in green and again this point is matched fit the fit at the same frequency. The arrow between the desired $\mathrm{f_0}$ and trimmed KID point represents the length of IDC fingers that must be trimmed dL on the y-axis. Bottom left then shows the calculated dL for all KIDs including a control group at low frequencies and a $80\,\mathrm{nm}$ offset to compensate for any error in alignment. Bottom right showing a segment of an IDC in the KLayout software. The designed E-beam pattern shown in red, the filled in red is intended overlap between the pattern and the finger. This small overlap corresponds with the calculated trim length for that KID.

Specifically the dL's are found as follows. After mapping a fabricated array, all $\mathrm{f_0}$'s are plotted against the designed total fingers lengths L. SEM analysis showed IDCs are produced with an accuracy better than $0.1\,\mu\mathrm{m}$, so the plot in figure 4.8 (a) can reasonably be taken as accurate. A simple least squared fit of a third degree polynomial is drawn through the plot. To simulate IDC trimming, KIDs can be moved over this fit. However, figure 4.8 (b) shows how KIDs are not placed perfectly on the fitted curve so before we can simulate trimming each KID is matched with the point on the curve which matches its $\mathrm{f_0}$. Before analysing further we remember all KIDs will be trimmed at least $80\,\mathrm{nm}$, so every point is moved down along the curve until it L has dropped by that amount. Now the data set is ready for variable trimming simulations. We then find which KIDs need to be trimmed by checking if the frequency spacing $\mathrm{df_0}$ respects the yield criterion. This experiment is done on a 400 KID array on a bandwidth of $4.1-7.9\,\mathrm{GHz}$ with a $0.2\,\mathrm{GHz}$ gap in the middle for the local resonator. A maximum $\mathrm{df_0}$ of $9\,\mathrm{MHz}$ can be achieved over the whole array. Of 400 designed KIDs, 395 were detected. The first 94 KIDs,

up to frequencies of $5.1\,\mathrm{GHz}$ are taken as a control group and are not trimmed. The remaining 301 mapped KIDs checked for a minimal $\mathrm{df_0}$ of $7\,\mathrm{MHz}$. This value was chosen such that roughly half of the experimental group of KIDs are variably trimmed. If a KID needs to be trimmed it is moved along the frequency axis until it has a $\mathrm{df_0}$ of $7.5\,\mathrm{MHz}$ relative to its left side neighbour, represented by the yellow to green arrow in figure 4.8 (c). After each move the data set is updated with the new desired $\mathrm{f_0}$ to make sure that no problems can be caused by moving a KID too close to its right side neighbour. After all KIDs have been checked and moved, all moved KIDs are again matched with a point on the fitted curve at their new $\mathrm{f_0}$. In this case 177 KIDs are moved, the remaining 122 KIDs in the experimental group of KIDs are trimmed only by $80\,\mathrm{nm}$. The difference in total finger length between the two matched points on the curve gives the trim length dL. This process is visualised in figure 4.8 (c).

Figure 4.8 (d) finally shows the calculated dL with the described algorithm, including the control group below $5.1\,\mathrm{GHz}$ and a dL of $80\,\mathrm{nm}$ for 'untrimmed' beyond that. Note how higher frequency KIDs on average have a lower dL. This effect is likely a consequence of the inverted square root relation between capacitance and $\mathrm{f_0}$. It seems that the largest dL's in figure 4.8 (d) also show a square root-like characteristic. The assumption needed here to make these calculation valid is that the relation between total finger length and resonance frequency can be taken as linear in the regime between measured pre-trimmed KID points and their matched point on the fit.

5

Results

5.1. Pre-trim characterisation

The first step to characterise any array is to do a VNA scan without illumination and find the resonance frequencies as fabricated with a simple peak finding algorithm. These can not immediately be compared to the designed f_0's since some transmission dips will have switched position in frequency space. Before any data analysis can be done all dips are spatially mapped to a KID. The result of that mapping experiment for array LT361, chip 4, is plotted in figure 5.1 together with the normalised error of the resonance frequency $\delta\mathrm{f}/\mathrm{f}$ with respect to a scatter-free array. The standard deviation of these errors over the array is the frequency scatter.

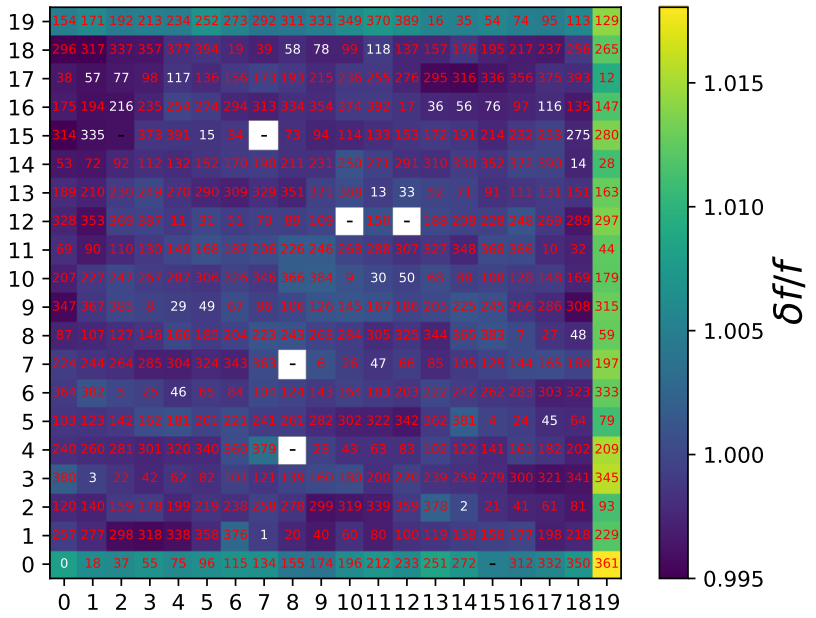

Figure 5.1: The spatially mapped LT361 400 KID array where 5 KIDs in the white spaces were either not identified or malfunctioning. Numbers show KID IDs in order of increasing resonance frequency. IDs are colored red if it does not match the designed ID for that position in the array. The color bar shows the normalised error in resonance frequency with respect to a scatter-free array. Two KIDs in the array were mapped in this experiment but are lost post-trimming, so they are not given an ID here.

A clear boundary effect on three out of four edges on the array is observed with the strongest effect on the right edge. Out of 395 detected transmission dips, all 395 were mapped to a KID, five spaces are blank, most likely because the KID was malfunctioning and not showing a dip in the VNA scan. A frequency scatter of $\sigma_{\delta\mathrm{f}/\mathrm{f}} = 3.9 \times 10^{-3}$ and a yield of $95.4\,\%$ are found. Yield is here again defined as

the fraction of KIDs with more than a $0.94\,\mathrm{MHz}$ spacing to their right-side neighbour. To get a sense of the scatter within the bulk of the array we look to figure 5.2 where f-scatter is plotted against measured resonance frequencies.

Monte-Carlo simulations performed in chapter 2 for a 400 pixel array and the same frequency scatter predicted a yield of $92.4\,\%$. The statistical nature of scatter means the measured yield of one array will almost never match the prediction exactly. A slight increase in yield may be a consequence of the edge effect in the array. The edges deviate strongly from the normal distribution in the bulk of the array as we will see in figure 5.10 (b).

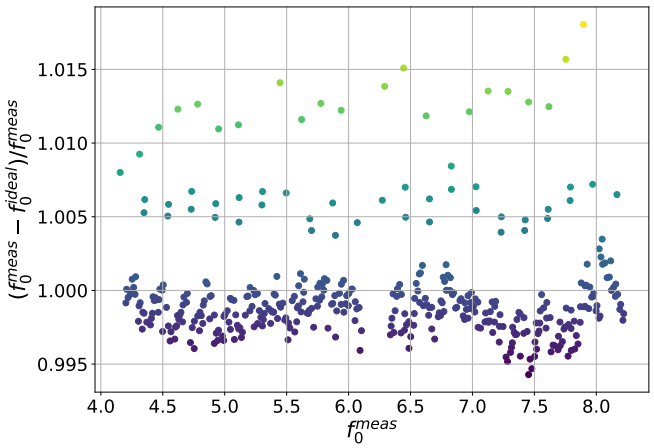

Figure 5.2: The measured frequency scatter against the measured resonance frequency of each KID in the LT361 array. The color of the data points matches the colorbar in figure 5.1.

All mapped KIDs have a known designed total IDC finger length L that can now be matched to a measured $\mathrm{f_0}$, creating the red curve in figure 5.3. Looking closely at the data, periodic outliers to the bottom of the curve are seen. This is again a different way to see the edge effect, only the shift in resonance of the left edge is large enough to be spotted here. The data closely follows values predicted by SONNET simulations, represented with blue points. There is a frequency dependant increase in $\mathrm{f_0}$ in the fabricated array, with a bigger shift for larger $\mathrm{f_0}$'s.

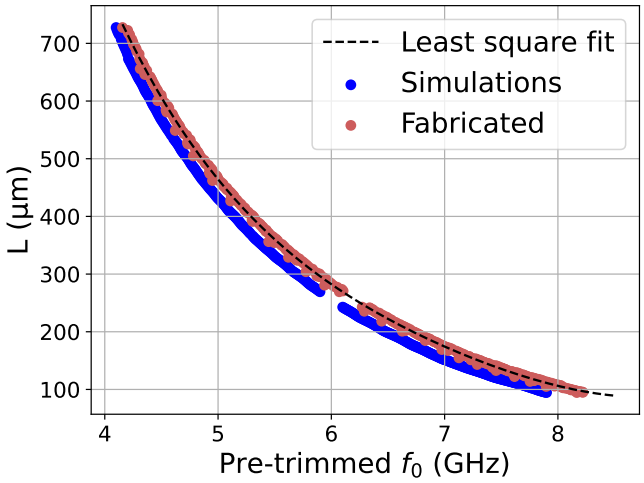

Figure 5.3: A graph showing the measured $\mathrm{f_0}$'s of the LT361 array before trimming against the designed total IDC finger length, together with the least square fit used for the trimming algorithm. Measured $\mathrm{f_0}$'s can be compared with expected values from SONNET simulations.

A least square fit through the measured points is also given in this figure by a dashed black curve. The trimming algorithm uses this fit to calculate what length of IDC fingers to remove.

5.2. Scatter analysis

Four cooldown experiments have been performed on the older LT343 array as described in chapter 4, with one dark VNA scan each. The first cycle was cooled from room temperature to $0.1\,\mathrm{K}$. The second warmed up to $175\,\mathrm{K}$ and cooled back down. For the third cycle the array was warmed to $21.8\,\mathrm{K}$ and finally to $26.4\,\mathrm{K}$ for the fourth cooldown cycle. The frequency scatter results from measuring the average shift $\delta \mathrm{f}_0$ in f_0 over the cycles with respect to a previous dark measurement for every transmission dip. A value of $\sigma_{\delta \mathrm{f/f}} = 8.4 \times 10^{-7}$ was calculated. We conclude the effects of the experimental setup and any change in the KIDs themselves between measurements do not have a significant effect on the scatter and will not limit the achievable array size. This result also gives assurance that measurements done with these array will be reproducible.

SEM images from specifically IDC's in the LT343 array have been analysed and the results can be found in table 5.1. Results can be compared to tolerances of a similar array (LT192), fabricated with only EUV lithography and the DESHIMA filter bank [32]. The filter bank is a usefull comparison because it also fabricated with EBPG and superconducting materials, using a $20\,\mathrm{nm}$ E-beam diameter. For width line W and length L we distinguish three relevant values each. <W> is the average width of all IDC fingers, which was designed to be $3\,\mu\mathrm{m}$. The length of the imaged IDC fingers was $8\,\mu\mathrm{m}$ so fabricated tracks came out slightly under $1\,\%$ smaller than intended in both dimensions. This was adjusted for in the fabrication of the LT361 array. $\sigma_{<\mathrm{W}>}$ is the standard deviation of the average measured IDC finger widths between KIDs while σ_{W} is the standard deviation of the width within one finger. For calculating the f-scatter introduced by fabrication tolerances $\sigma_{<\mathrm{W}>}$ and $\sigma_{<\mathrm{L}>}$ are substituted in the graphs of figure 3.5.

Table 5.1: Average line dimensions and fabrication tolerances compared between two LEKID arrays and the DESHIMA filter bank obtained from previously described edge detection algorithm. All values are in nanometers. Some of the SEM images used to calculate these values for all three samples can be found in appendix A

	LT343	LT192	DESHIMA
$< \mathrm{W} >$	2975	1583	1819
σ_{W}	10.52	13.48	12.03
$\sigma_{<\mathrm{W}>}$	8.448		7.932
$< \mathrm{L} >$	7921		
σ_{L}	8.556		
$\sigma_{<\mathrm{L}>}$	55.07		

No length analysis was done for finger lengths in the LT192 chip or DESHIMA. The reason being the LT192 KIDs have poorly defined ends of fingers, making measuring the length ambiguous at the SEM pixel level and DESHIMA filter banks do no have a track length that can be measured in a single SEM image. $\sigma_{<\mathrm{W}>}$ is also missing for the LT192 array because not enough close-up SEM images of those IDCs have been made. For analysis of array LT343 $\sigma_{\delta \mathrm{f/f,W}} = 0.78 \times 10^{-3}$ and $\sigma_{\delta \mathrm{f/f,L}} = 0.36 \times 10^{-3}$ are found and used in equation 3.4 to give a final f-scatter of $\sigma_{\delta \mathrm{f/f,IDC}} = 0.86 \times 10^{-3}$

It should be noted that there is less data available to calculate a standard deviation $\sigma_{<\mathrm{W}>}$ or $\sigma_{<\mathrm{L}>}$ than we might wish. Because SEM imaging of KIDs is a time intensive process only 10 separate IDCs in the LT343 array have been imaged.

5.3. Post-trim Characterisation

The LT361 array that was previously mapped in figure 5.1 is subjected to the trimming algorithm described in chapter 4, to determine what IDCs to trim and by how much. All KIDs with an f_0 lower than $5.1\,\mathrm{GHz}$ are taken as a control group to measure any effect the post-processing has on the array without trimming. In the experimental group, all KIDs are trimmed by $80\,\mathrm{nm}$ to compensate for E-beam

misalignment and this is accounted for by the algorithm before trim lengths dL are calculated. Only KIDs with a $\mathrm{df_0}$ of less than $7\,\mathrm{MHz}$ are trimmed with a variable dL. Of the 395 mapped KIDs, 92 are part of the control group, 122 are trimmed by $80\,\mathrm{nm}$ and 181 are trimmed by more. Figure 5.4 shows a segment of VNA scans of the LT361 array before and after trimming. The same bandwidth is shown in the top and bottom figures.

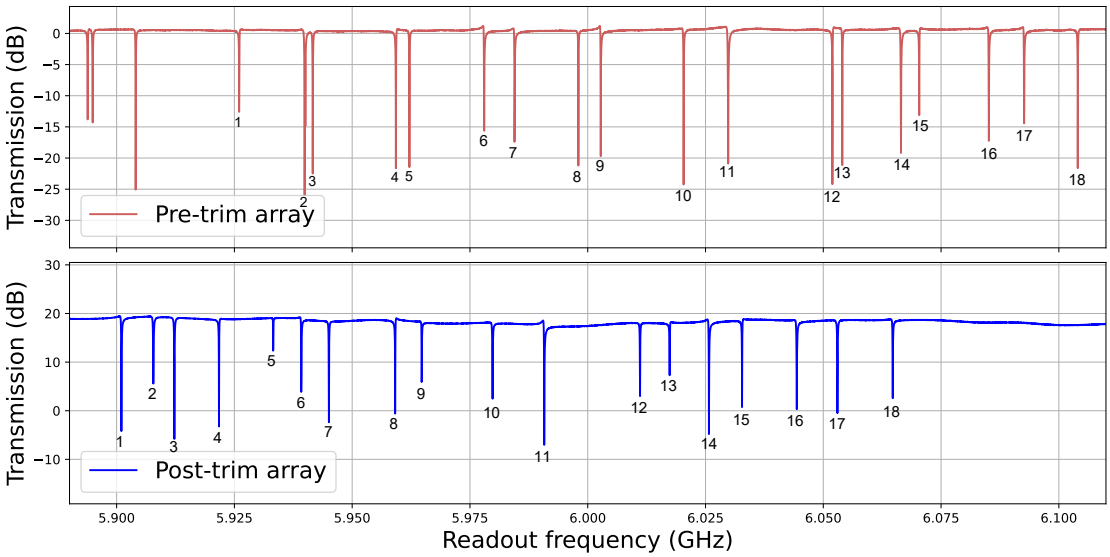

Figure 5.4: A segment of VNA scans of the same array before (top) and after (bottom) a trimming experiment. The dips that correspond with the same KIDs have been numbered in both graphs. Note how the $\mathrm{f_0}$'s have shifted down relative to their pre-trim values.

The transmission dips corresponding to the same KID in both scans have been numbered so their shift can more easily be tracked. The post-trim array shows a clear improvement in frequency spacing. Note how the spacing is still not uniform since only KIDs with less than $7\,\mathrm{MHz}$ between them before trimming should have shifted significantly. Large gaps between transmission dips such as between dips 11 and 12 in figure 5.4 will remain. To see the $\mathrm{df_0}$'s in the whole array we go to figure 5.5.

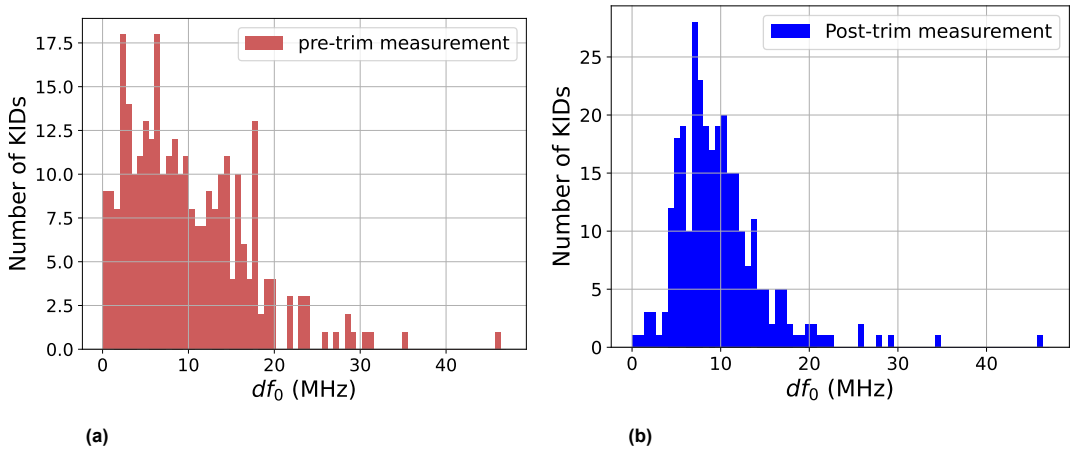

Figure 5.5: Left histogram showing frequency spacing $\mathrm{df_0}$ of only the trimmed KIDS in the LT361 array before trimming. The right image showing frequency spacing of the same array after trimming.

These two histograms exclude the untrimmed control group to accurately represent the result of the trimming experiment. The spacing histogram has significantly changed from a broad distribution to a sharper one centered around the $7.5\,\mathrm{MHz}$ which the algorithm tried to achieve. The trimmed array still contains 1 KID with a $\mathrm{df_0} < 11.6$ linewidths. To be able to say more about the trimming results the array

needs to be mapped again. Otherwise, since we do not yet know the scatter induced by the trimming process, we can not be certain that no transmission dips swapped positions in frequency space. The post-trim mapping result is given in figure 5.6 by another frequency error map.

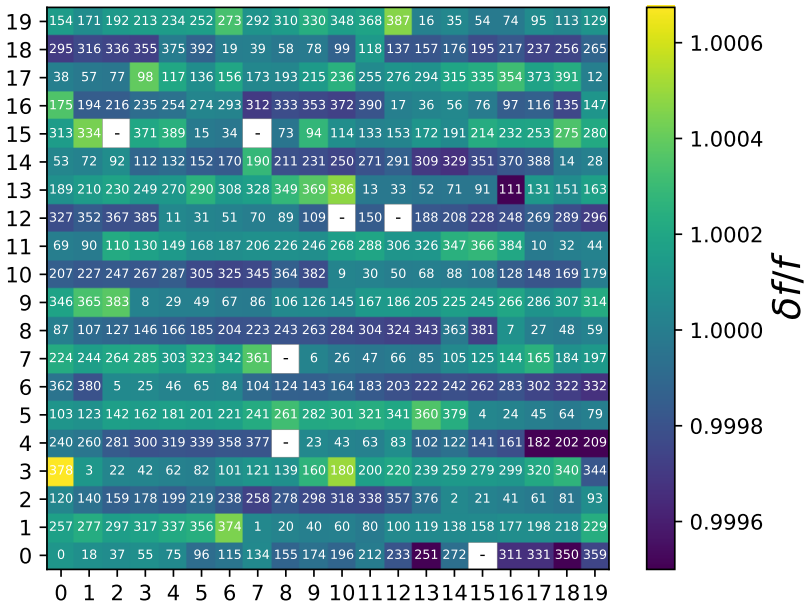

Figure 5.6: Left figure showing a spatial map of the normalised frequency error for the LT361 array before IDC trimming. Right figure showing the same error for that array after IDC trimming. After trimming, besides the five eliminated KIDs, two KIDs were failed to be identified during the mapping experiment. The improvement in f-scatter is already noticeable by the different scale of the colorbar for frequency error compared to figure 5.1

Post-trimming only 393 KIDs were identified, meaning 2 additional KIDs were lost during post-processing or missed in the mapping measurements. The edge effect visible in figure 5.1 are not visible post-trimming. The absolute shift in resonance frequencies is still there but now here the frequency error is relative to the pre-trim measurements while the pre-trim frequency error was relative to the designed f_0's. Looking closely at figure 5.6 an alternating pattern for each row is discovered. To see this more clearly, figure 5.8 was made by plotting the frequency errors of the post-trim array against f_0.

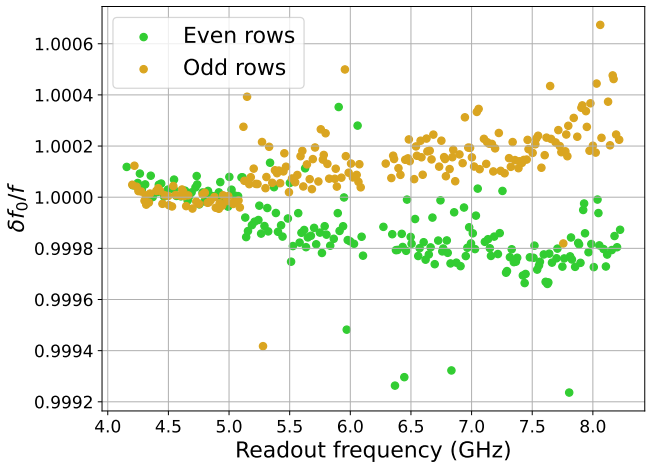

Figure 5.7: A graph showing normalised frequency error in the LT361 array after IDC trimming like in figure 5.2 , making a distinction between even numbered and odd numbered rows as numbered in figure 5.6.

For $f_0 < 5.1\,\mathrm{MHz}$, even and odd numbered rows, as numbered in figure 5.6 show little to no difference,

in stark contrast to the trimmed KIDs. Misalignment of the E-beam along the length of the IDC fingers gives a plausible explanation as to why odd and even rows scatter differently. Even numbered rows the ends of their trimmable IDC fingers pointed in positive y-direction while odd numbered rows have their fingers pointed toward negative y-direction. A misalignment of the E-beam towards positive y then means odd rows get trimmed more, making their resonance frequencies to increase more than expected, as we see in figure 5.8.

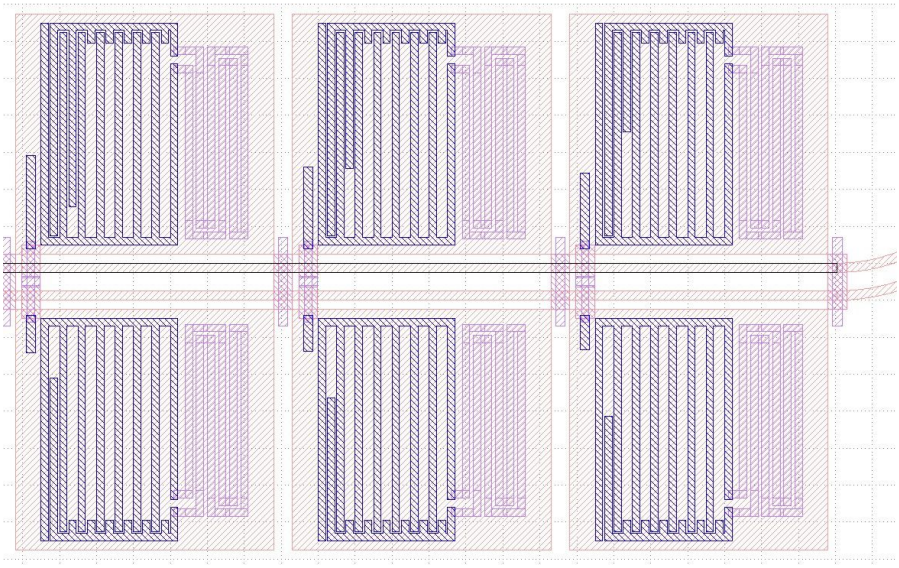

Figure 5.8: Snapshot taken from the bottom two rows (rows 0 and 1 in figure 5.6) of the LT361 array in KLayout software. Even numbered rows have incomplete IDC fingers pointed towards positive y-direction, while odd numbered rows have IDC fingers pointed towards negative y-direction. If there is a misalignment of the E-beam y-direction, each row will have an opposite error in trimmed length.

After mapping the array again after trimming, the shift in resonance frequency of every transmission dip can also be determined. This resulted in figure 5.9 (b). The result is compared to the prediction made by the trimming algorithm infigure 5.9 (a).

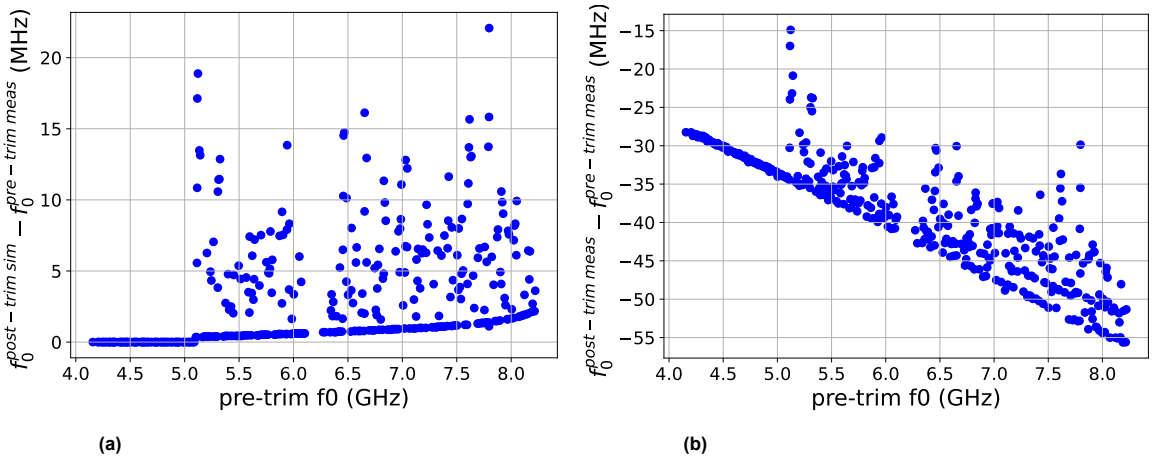

Figure 5.9: Left image showing the predicted shift of resonance frequencies after trimming. Right image showing the measured shift of resonance frequencies after trimming, clearly showing a linear frequency dependence.

The trimming of IDC fingers alone can only move transmission dips up in frequency. An unexpected, frequency dependant shift has affected the array which has moved the whole array between 28 and $56\,\mathrm{MHz}$ down. Most likely the material properties of $\beta - \mathrm{Ta}$ and NbTiN have changed slightly during

baking, etching and cleaning of the array. If kinetic inductance $\mathrm{L_k}$ has increased for example, we would indeed see a decrease in $\mathrm{f_0}$ like we see in figure 5.9 (b). In that plot the two separated groups in trimmed KIDs are also apparent, with one group staying in a straight line with the control group and the other group bending towards higher frequencies.

Finally we can calculate the achieved frequency scatter in the post-trim array. Only taking the trimmed group of KIDs into account, a value of $\sigma_{\delta \mathrm{f/f}} = 0.21 \times 10^{-3}$ is found. To get a sense of how this compares to the pre-trim array we go to figure 5.10 where the frequency errors are plotted as both scatterplots and histograms. Again we should note that frequency errors in the pre-trim array are calculated with respect to the designed $\mathrm{f_0}$'s from SONNET simulations and post-trim frequency errors with respect to pre-trim measured $\mathrm{f_0}'\mathrm{s}$.

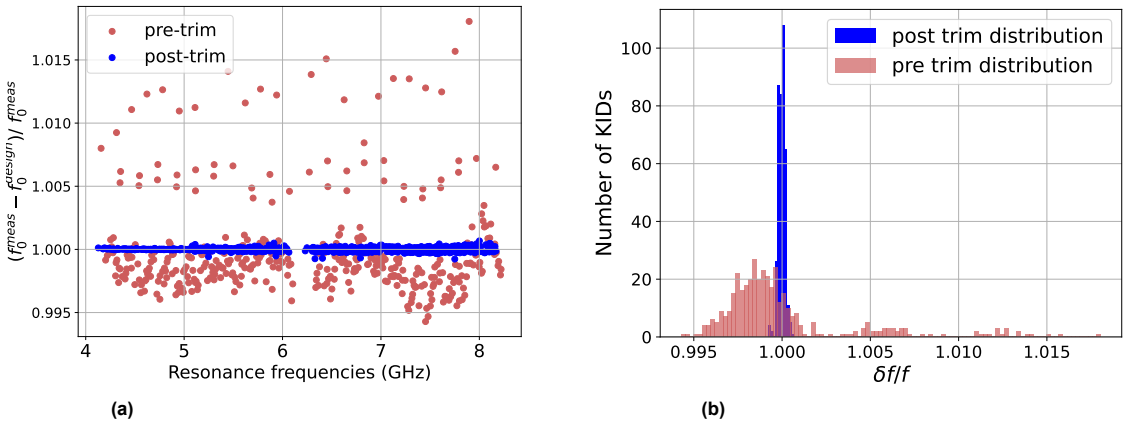

Figure 5.10: Left image showing the relative difference between designed and measured resonance frequencies of mapped KIDs before and after trimming. Right image showing histograms of normalised frequency errors over the whole LT361 array before and after IDC trimming with $\sigma_{\delta \mathrm{f/f}} = 3.9 \times 10^{-3}$ and $\sigma_{\delta \mathrm{f/f}} = 0.21 \times 10^{-3}$ respectively.

The yields and frequency scatter of the LT361 array pre- and post-trimming are summarised in table 5.2. Starting from an array design with 400 KIDs, in the first dark VNA scan of the initially fabricated array, 395 transmission dips were found. After trimming and disabling the 5 unmapped KIDs, 393 transmission dips were found in another dark VNA scan. We can see however that the spatial mapping setup is able to match $100\,\%$ of dips to a KID in the array. The fact that the achieved frequency scatter in the post-trim array is so close to the desired $\sigma_{\delta \mathrm{f/f}} = 0.2 \times 10^{-3}$ is a promising result and proves that IDC trimming can almost definitely be used to reliably create 1000 MUX LEKID arrays. It should then however also be taken into account that fabrication yield or imperfect data analysis is a significant factor. In this case yield in the final array was decreased by $1.75\,\%$.

Table 5.2: Summary of f-scatter and yield results. Fabrication yield is the number of transmission dips found in a dark VNA scan. Mapping yield is the number of transmission dips spatially mapped to a KID in the array. Post-trim $\sigma_{\delta \mathrm{f/f}}$ has been calculated using only the experimental group of KIDs which were trimmed by at least $80\,\mathrm{nm}$ rather than the whole array.

	Pre-trim	Post-trim
Designed array size	400	395
Fabrication yield	395	393
Mapping yield	395	393
$\sigma_{\delta \mathrm{f/f}}$	3.9×10^{-3}	0.21×10^{-3}

5.4. Quality factor fitting

Separate high resolution VNA scans were performed for every transmission dip in both the pre- and post-trimmed LT361 array. A signal power of $-110\,\mathrm{dBm}$ is used for these scans. An algebraic fit is performed on all these dips. All fits should look like the example seen in section 4.2. $\mathrm{Q_C}$'s are extracted from resonance circles and plotted in figure 5.11.

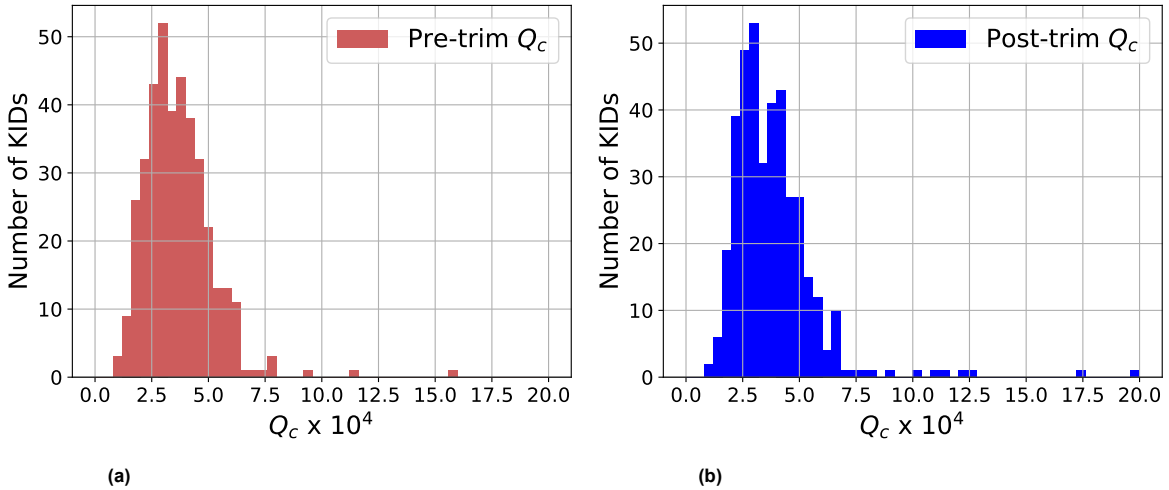

(a) (b)

Figure 5.11: Left showing the histogram resulting from fitting transmission dips in the pre-trimmed LT361 array from high resolution scans and extracting $\mathrm{Q_c}$. Right showing the same histogram for the post-trim LT361 array. broad distribution with $\sigma_{\mathrm{Q_c}}$ = 1.2×10^4 are found for both arrays.

The array was designed to have a constant $\mathrm{Q_c}$ of 5×10^4 over the whole array. The fabricated arrays have a lower average $\mathrm{Q_c}$ of 3.56×10^4. Clearly not only resonance frequencies are scattered in a real array but quality factors as well. The distribution of quality factors in figure 5.11 are quite broad but consistent between the pre- and post-trimmed array. Q-scatter is found by calculating the standard deviation of the data in these histograms. Pre-trim we find $\sigma_{\mathrm{Q_c}}$ = 1.20×10^4 and post-trim we find $\sigma_{\mathrm{Q_c}}$ = 1.22×10^4, which is not a significant increase.

6

Discussion

6.1. Frequency scatter analysis

From the VNA scans only the total frequency scatter can be determined. Resonance frequencies in a 400 KID array were mapped to their corresponding KIDs. A n f-scatter of $\sigma_{\delta \mathrm{f/f}}$ = 3.9×10^{-3} was calculated. Different sources of f-scatter can not be distinguished from simply looking at this data. Two possible sources of f-scatter have been studied, namely the effects of the measurement setup and the effects of variations in IDC finger dimensions. The contribution of the measurement setup was determined to be $\sigma_{\delta \mathrm{f/f}}$ = 8.4×10^{-7}. We conclude that no significant scatter occurs between cooldown cycles. That is not to say that some scatter may occur over longer periods of time, for example due to a slow change in material properties. From this value we do conclude that measurements done with these arrays are reproducible.

KID fabrication was reliable and accurate up to $\sigma_{\delta \mathrm{f/f}}$ = 0.86×10^{-3} based on deviation in IDC finger dimensions between KIDs. Scatter caused solely by IDC fabrication is already a factor 4 higher than the $\sigma_{\delta \mathrm{f/f}}$ = 0.2×10^{-3} we are aiming for. Close-up SEM images were also made of some inductors and edge-detection on these images was attempted. Unfortunately the contrast between $\beta - \mathrm{Ta}$ and the sapphire substrate was insufficient for either ProSEM or the edge-detection algorithm described in chapter 3 to determine the line dimensions. Let us assume the frequency scatter introduced by fabrication tolerance on the inductor introduces the same frequency scatter as the IDC. It is presumable that at least the tolerance on line dimensions are the same in the inductor and the IDC since both are written with the same E-beam technique. Including the inductor then raises the introduced f-scatter to $\sigma_{\delta \mathrm{f/f}}$ = 1.22×10^{-3} or just under a third of the scatter found in the array. All components of a KID affect performance. For example, changes in coupler bar and ground plane distance to the IDC, will alter the capacitance of a KID. Tolerances on all components will add to f-scatter. We assume the IDCs and inductors to have the most critical dimensions. We experimentally showed that the measurement setup does not significantly contribute to f-scatter so clearly there are other sources of f-scatter to be found.

It should be mentioned that the pre-trim f-scatter calculation did not take the boundary effect on the array into account. The $\delta \mathrm{f/f}$ with respect to the least square fit of every KID was bunched together and the standard deviation over the whole array was taken. In this way the boundary effect will add to the f-scatter. Leaving out the edges pre-trimming gives $\sigma_{\delta \mathrm{f/f}}$ = 1.41×10^{-3}, which would mean f-scatter in most of the array is almost entirely caused by fabrication tolerances.

An easy conclusion to draw from these values is that fabrication must be improved in order to meaningfully decrease f-scatter. We can use the model used to make figure 3.5 and translate a required frequency scatter of $\sigma_{\delta \mathrm{f/f}}$ = 0.2×10^{-3}, to an acceptable fabrication tolerance. For this calculation, IDC width tolerance $\sigma_{<\mathrm{W}>}$ is taken as the only variable. We arrive at a maximal acceptable tolerance of $\sigma_{<\mathrm{W}>}$ = $4.01\,\mathrm{nm}$. This is less than half of the current tolerance on IDC finger width. If we include

the effects of length and other components this value will decrease even further. Sub-nm fabrication tolerance has been achieved before in semiconductor chip manufacturing [33], but never using superconducting materials.

There are suggestions to be made to improve fabrication accuracy. We could use a finer E-beam to write the inductors and IDCs of KIDs. The DESHIMA filter banks in table 5.1 were written using a $20\,\mathrm{nm}$ E-beam, whereas our KID arrays use a $10\,\mathrm{nm}$ E-beam diameter. Comparing the two no improvement was made by using a finer beam. Fabricating KIDs with sufficiently accuracy may not be possible with the current EBPG technology. Until large improvements can be made, post-processing techniques will remain necessary.

6.2. Achievable array size

Looking back at chapter 2, a KID response model was used to determine the minimal frequency spacing df_0 between transmission dips was needed to always have less than -$10\,\mathrm{dB}$ cross talk in the array due to frequency collisions. We found df_0 needed to be at least $0.94\,\mathrm{MHz}$ for KIDs with a resonance frequency near $4\,\mathrm{GHz}$ and quality factor Q = 5.0×10^4. On a 4-$8\,\mathrm{GHz}$ bandwidth, that means an absolute theoretical maximum array size of 4264 KIDs. Later in chapter 2 more practical limitations were discussed. The yield of an array was defined as the fraction of KIDs which have at least the required $0.94\,\mathrm{MHz}$ frequency spacing to their right-side neighbour in frequency space. We saw the presence of frequency scatter can significantly decrease yield. At the start of this thesis the goal was set to enable the fabrication of a 1000 MUX array with an expected yield of $95\,\%$. With a trimming experiment the frequency scatter was reduced to $\sigma_{\delta \mathrm{f/f}}$ = 0.21×10^{-3} With a relatively simple algorithm we were able to accurately predict the change in resonance frequency from a small change in IDC finger length. Interestingly, knowing the actual capacitance of a KID was not needed. The experimental data, combined with designed total IDC finger length, is enough to achieve a large improvement in yield. According to our model and Monte-Carlo analysis this enables fabrication of $95\,\%$ yield arrays of around 980 KIDs. We take a closer look at some design choices and discuss how array size might be increased further.

Measured yield in the pre-trimmed array in the results was comparable but slightly higher than predicted. Possibly due to the boundary effect offsetting KIDs at three edges of the array and the frequency dependent increase in f_0 compared to the SONNET simulations in figure 5.3. Because of this increase the array takes up a larger bandwidth than designed, meaning the average df_0 must have increased, raising the yield.

The requirement on df_0 is based on a maximum phase response of the KIDs in the LT361 array. The design of the inductor may be adjusted to decrease the response magnitude. By increasing the total volume of an inductor a lower fraction of the total Cooper pairs are broken into quasiparticles and the transmission dip will move less. As a result the neighbouring KID won't experience as much cross talk due to frequency collisions as in the current array. A less stringent requirement is put on df_0 for lower responses. While a suppressed response may be advantageous for the MUX factor we reach, the resolving power of KIDs will suffer from such an inductor design. Currently there is no clear optimal desired response for KIDs and a choice must be made for every design to balance resolving power with multiplexability.

Another idea that was floated is to significantly increase Q_c to make transmission dips less wide. Keeping in mind that the total Q needs to be dominated by Q_c in equation 2.8 puts a limit in how far we can push this. Q_c is a lot easier to control than Q_i which depends on, among other things, quasiparticle dynamics as well and phonon losses. Also changing quality factors has an impact on KID response so again a balance between response and dip width can be considered.

The last design suggestion to increase achievable array size is to simply increase the bandwidth an array occupies. Keeping df_0 the same, the achievable KID size increases linearly with bandwidth. Now first of all, we came across a very practical upper limit on the bandwidth as it turns out the VNA readout is limited to a maximum frequency of $8.5\,\mathrm{GHz}$.

The frequency dependent decrease in f_0 seen in figure 5.9 (b) might be used to our advantage in future trimming experiments. If it turns out the shift observed here is consistently reproducible, then we just found a way to both decrease and increase f_0 with just one experiment. More sophisticated trimming algorithms can then be made which take these shifts into account to make arrays with highly uniform df_0's. Before applying such algorithm the unexpected f_0 decrease needs to be accurately modelled or measured in many more arrays. Most likely the shift is highly dependent on exactly how post-processing is performed. For example baking resist at different temperatures or for a different length of time may change the perceived shift.

6.3. Q-factor mismatch

Trimming may be applied to coupler bars to adjust quality factor Q in a very similar way as was done with resonance frequencies. Quality factors have also been simulated in SONNET and have a strong dependence on f_0 and coupler bar length $\mathrm{L_c}$. Again the structures in a KID can only decrease in size. A decrease in $\mathrm{L_c}$ results in a increase in $\mathrm{Q_c}$. Fitted Q-factors were lower than designed, so trimming the coupler bar could improve array performance even further. A simultaneous coupler bar and IDC trimming experiment was considered for this thesis, but it was decided against. It is good practice to keep the variables in an experiment to a minimum. The frequency shift can now be more clearly attributed to our capacitor trimming and possible changes in material properties, rather than changes made to the coupler bar.

SONNET simulations show that there is also a weak relation between IDC finger length and $\mathrm{Q_c}$. Especially the number of IDC fingers in a KID have an effect on coupling. From figure 5.11 it became clear that IDC trimming has very little effect on $\mathrm{Q_c}$. Assuming that changing $\mathrm{L_c}$ also has no significant effect on the capacitance of a KID these two trimming experiments can be executed simultaneously with completely separate calculations. However, it should be kept in mind that post-processing of arrays is not a panacea for array performance. The sources of Q-scatter should be further investigated as f-scatter has in this thesis and other literature.

6.4. Research recommendations

The trimmed KID array has a frequency scatter of $\sigma_{\delta \mathrm{f}/\mathrm{f}} = 0.2 \times 10^{-3}$. In figure 2.9 (b) the array is then located in the steepest part of the graph defining the achievable MUX factor. Any improvement to the trimming algorithm or process here will be significant and is certainly worth investigating. The first step could be to look into better counteracting the misalignment to further decrease f-scatter.

The $-10\,\mathrm{dB}$ requirement on frequency collisions was chosen somewhat arbitrarily. For future arrays a more meaningful value should be chosen. One suggestion to decide what the requirement should be is to make sure that the resolving power of a device is never limited by frequency collisions.

The response model takes the designed inductor volume as an input to calculate response. The magnitude of response the model gives was not compared to accurate measurements of KID response on the arrays. KID response should be measured using a monochromator so our model can be calibrated to more accurately represent KIDs in a certain array. The response model can become a tool for determining yield criteria.

7

Conclusions

This thesis aims to answer two questions: "**What is the theoretical limit on the MUX factor in single readout line KID devices while retaining a 100 % yield?**" and "**How much can array yield be improved using post-processing techniques?**". The goal was set to, if possible, enable the fabrication of KID arrays with a 1000 MUX factor, on a 4-$8\,\mathrm{GHz}$ bandwidth and a constant quality factor $\mathrm{Q} = 5.0 \times 10^4$. First the response of optical KIDs to a high energy photon was modelled in chapter 2 and the effect of frequency collisions were explored. The measured photon energy of a KID is highly dependent on the state of its right-side frequency neighbour. To keep the cross talk from these collisions below $-10\,\mathrm{dB}$ a minimal frequency spacing of $0.94\,\mathrm{MHz}$ is determined for KIDs with $\mathrm{Q} = 5.0 \times 10^4$ and resonance frequencies near $4\,\mathrm{GHz}$. On a 4-$8\,\mathrm{GHz}$ bandwidth that results in a theoretical maximum MUX factor of 4264. Statistical analysis showed a maximal frequency scatter of $\sigma_{\delta \mathrm{f}/\mathrm{f}} = 0.2 \times 10^{-3}$ can be allowed to have a 1000 KID array where a yield of $95\,\%$ can be expected. Before trimming, the f-scatter measured in a 400 LEKID array was $\sigma_{\delta \mathrm{f}/\mathrm{f}} = 3.9 \times 10^{-3}$. This value is inflated by a boundary effect in the array. Three out of four edges of the array have significantly shifted resonance frequencies with respect to the bulk of KIDs. Ignoring these edges out, a frequency scatter of $\sigma_{\delta \mathrm{f}/\mathrm{f}} = 1.41 \times 10^{-3}$ was calculated.

Some possible sources of f-scatter were mentioned in chapter 3 and chapter 4. The measurement setup itself was experimentally found to not contribute significantly. An array design where frequency neighbours are spatially far apart makes us believe we can assume an insignificant electromagnetic contribution to f-scatter as well. Fabrication tolerances were measured in IDC fingers and the effect on f_0 is modelled. From here an f-scatter of $\sigma_{\delta \mathrm{f}/\mathrm{f}} = 0.86 \times 10^{-3}$ is calculated. Assuming a similar effect as a result of inductor tolerance, we get $\sigma_{\delta \mathrm{f}/\mathrm{f}} = 1.22 \times 10^{-3}$. It is concluded that most frequency scatter is caused by variations in line dimensions. To reach the required $\sigma_{\delta \mathrm{f}/\mathrm{f}} = 0.2 \times 10^{-3}$ post-processing is required.

A post-processing technique is proposed in chapter 4 where IDC fingers are trimmed to adjust the resonance frequencies in a second round of lithography. In the post-trimmed, 400 KID array an f-scatter of $\sigma_{\delta \mathrm{f}/\mathrm{f}} = 0.21 \times 10^{-4}$ is measured. An improvement of nearly a factor 18 compared to the same array before trimming. Using the statistical model from chapter 2 we expect an array size of 980 KIDs, with $95\,\%$ yield, to be achievable with this trimming technique. Resonance frequencies can only be increased by trimming. However, in the results we observed a drop in resonance frequencies across the array after trimming. An increase of kinetic inductance is the suspected cause. These effects may be exploited to improve the trimming algorithm and further raise the MUX factor.

Bibliography

[1] L. Kaltenegger and Z. Lin, "Finding signs of life in transits: High-resolution transmission spectra of earth-line planets around fgkm host stars," 2021.

[2] H. J. Deeg and R. Alonso, "Transit photometry as an exoplanet discovery method," *arXiv preprint arXiv:1803.07867*, 2018.

[3] S. Steiger, L. Pueyo, E. H. Por, P. Chen, R. Soummer, R. Pourcelot, I. Laginja, and V. P. Bailey, "Simulated performance of energy-resolving detectors towards exoplanet imaging with the habitable worlds observatory," in *Space Telescopes and Instrumentation 2024: Optical, Infrared, and Millimeter Wave*, vol. 13092, pp. 566–577, SPIE, 2024.

[4] A. Magniez, L. Bardou, T. Morris, and K. O'Brien, "Mkid: an energy sensitive superconducting detector for the next generation of xao systems," *Adaptive Optics Systems VIII], Schmidt, D., Schreiber, L., and Vernet, E., eds*, vol. 94.

[5] S. A. Taylor *et al.*, "Ccd and cmos imaging array technologies: technology review," *UK: Xerox Research Centre Europe*, pp. 1–14, 1998.

[6] K. Engelhardt and P. Seitz, "Optimum color filters for CCD digital cameras," *Applied optics*, vol. 32, no. 16, pp. 3015–3023, 1993.

[7] J. Baselmans, "Kinetic inductance detectors," *Journal of Low Temperature Physics*, vol. 167, pp. 292–304, 2012.

[8] G. Ulbricht, M. De Lucia, and E. Baldwin, "Applications for microwave kinetic induction detectors in advanced instrumentation," *Applied Sciences*, vol. 11, no. 6, p. 2671, 2021.

[9] X. Liu, W. Guo, Y. Wang, L. Wei, C. M. Mckenney, B. Dober, T. Billings, J. Hubmayr, L. Ferreira, M. Vissers, *et al.*, "Cryogenic LED pixel-to-frequency mapper for kinetic inductance detector arrays," *Journal of Applied Physics*, vol. 122, no. 3, 2017.

[10] P. Szypryt, S. Meeker, G. Coiffard, N. Fruitwala, B. Bumble, G. Ulbricht, A. Walter, M. Daal, C. Bockstiegel, G. Collura, *et al.*, "Large-format platinum silicide microwave kinetic inductance detectors for optical to near-ir astronomy," *Optics Express*, vol. 25, no. 21, pp. 25894–25909, 2017.

[11] S. Shu, M. Calvo, J. Goupy, S. Leclercq, A. Catalano, A. Bideaud, A. Monfardini, and E. F. Driessen, "Increased multiplexing of superconducting microresonator arrays by post-characterization adaptation of the on-chip capacitors," *Applied Physics Letters*, vol. 113, no. 8, 2018.

[12] E. Perinati, M. Barbera, S. Varisco, E. Silver, J. Beeman, and C. Pigot, "Experimental evidence of an incomplete thermalization of the energy in an x-ray microcalorimeter with a $\mathrm{Ta}/\ \mathrm{Au}$ absorber," *Review of scientific instruments*, vol. 79, no. 5, 2008.

[13] A. Coppolecchia, A. Paiella, L. Lamagna, G. Presta, E. Battistelli, P. de Bernardis, M. Castellano, F. Columbro, S. Masi, L. Mele, *et al.*, "W-band lumped element kinetic inductance detector array for large ground-based telescopes," *Journal of Low Temperature Physics*, vol. 199, no. 1, pp. 130–137, 2020.

[14] D. Wisbey, A. Martin, A. Reinisch, and J. Gao, "New method for determining the quality factor and resonance frequency of superconducting micro-resonators from sonnet simulations," *Journal of Low Temperature Physics*, vol. 176, pp. 538–544, 2014.

[15] P. J. De Visser, "Quasiparticle dynamics in aluminium superconducting microwave resonators," PhD thesis, Delft University of Technology, 2014.

[16] D. C. Mattis and J. Bardeen, “Theory of the anomalous skin effect in normal and superconducting metals,” *Physical Review*, vol. 111, no. 2, p. 412, 1958.

[17] D. M. Pozar, *Microwave engineering*. New York: John Wiley & Sons inc, 4th ed. 1998.

[18] A. Middleton, S. K. Choi, S. Walker, J. Austermann, J. R. Burgoyne, V. Butler, S. C. Chapman, A. T. Crites, C. J. Duell, R. G. Freundt, *et al.*, “CCAT: LED mapping and characterization of the 280 GHz TiN KID array,” *IEEE Transactions on Applied Superconductivity* preprint, 2024.

[19] K. Kouwenhoven, D. Fan, E. Biancalani, S. A. De Rooij, T. Karim, C. S. Smith, V. Murugesan, D. J. Thoen, J. J. Baselmans, and P. J. De Visser, “Resolving power of visible-to-near-infrared hybrid β-$\mathrm{Ta/Nb-Ti-N}$ kinetic inductance detectors,” *Physical Review Applied*, vol. 19, no. 3, p. 034007, 2023.

[20] O. Noroozian, P. K. Day, B. H. Eom, H. G. Leduc, and J. Zmuidzinas, “Crosstalk reduction for superconducting microwave resonator arrays,” *IEEE Transactions on Microwave Theory and Techniques*, vol. 60, no. 5, pp. 1235–1243, 2012.

[21] J. Baselmans. ’Private communication’.

[22] A. Pinto, V. Oliveira, and D. Falcão, “Miniaturization of direct alcohol fuel cells: Microfabrication techniques and microfluidic architectures,” pp. 245–264, Elsevier, 2018.

[23] R. Igreja and C. Dias, “Analytical evaluation of the interdigital electrodes capacitance for a multilayered structure,” *Sensors and Actuators A: Physical*, vol. 112, no. 2-3, pp. 291–301, 2004.

[24] N. Bhoedjang, “Evaluating frequency scatter in optical kinetic inductance detector arrays,” Bachelor’s Thesis, Delft University of Technology, 2023.

[25] K. Kouwenhoven, “Visible to near-infrared kinetic inductance detectors: Energy-resolving single photon detectors,” PhD thesis, Delft University of Technology, 2024.

[26] S. Probst, F. Song, P. A. Bushev, A. V. Ustinov, and M. Weides, “Efficient and robust analysis of complex scattering data under noise in microwave resonators,” *Review of Scientific Instruments*, vol. 86, no. 2, 2015.

[27] J. Gao, *The physics of superconducting microwave resonators*. California Institute of Technology, 2008.

[28] C. Hoek, “Analysis of frequency scattering in microwave kinetic inductance detectors,” Master’s Thesis, Delft University of Technology, 2024.

[29] M. Bottom, L. S. Neat, L. K. Harding, P. Morrissey, S. R. Meeker, and R. T. Demers, “Smartphone scene generator for efficient characterization of visible imaging detectors,” in *High Energy, Optical, and Infrared Detectors for Astronomy VIII*, vol. 10709, pp. 654–666, SPIE, 2018.

[30] G. J. Lomans, “Frequency scatter in kinetic inductance detectors: Improved analysis using pixel-to-frequency mapping setup,” Bachelor’s Thesis, Delft University of Technology, 2023.

[31] X. Liu, W. Guo, Y. Wang, M. Dai, L. Wei, B. Dober, C. M. McKenney, G. C. Hilton, J. Hubmayr, J. E. Austermann, *et al.*, “Superconducting micro-resonator arrays with ideal frequency spacing,” *Applied Physics Letters*, vol. 111, no. 25, 2017.

[32] A. Endo, P. Van der Werf, R. Janssen, P. De Visser, T. Klapwijk, J. Baselmans, L. Ferrari, A. Baryshev, and S. Yates, “Design of an integrated filterbank for deshima: On-chip submillimeter imaging spectrograph based on superconducting resonators,” *Journal of low temperature physics*, vol. 167, pp. 341–346, 2012.

[33] G. F. Lorusso, P. Leunissen, M. Ercken, C. Delvaux, F. Van Roey, N. Vandenbroeck, H. Yang, A. Azordegan, and T. DiBiase, “Spectral analysis of line width roughness and its application to immersion lithography,” *Journal of Micro/Nanolithography, MEMS and MOEMS*, vol. 5, no. 3, pp. 033003–033003, 2006.

A

SEM images of different devices

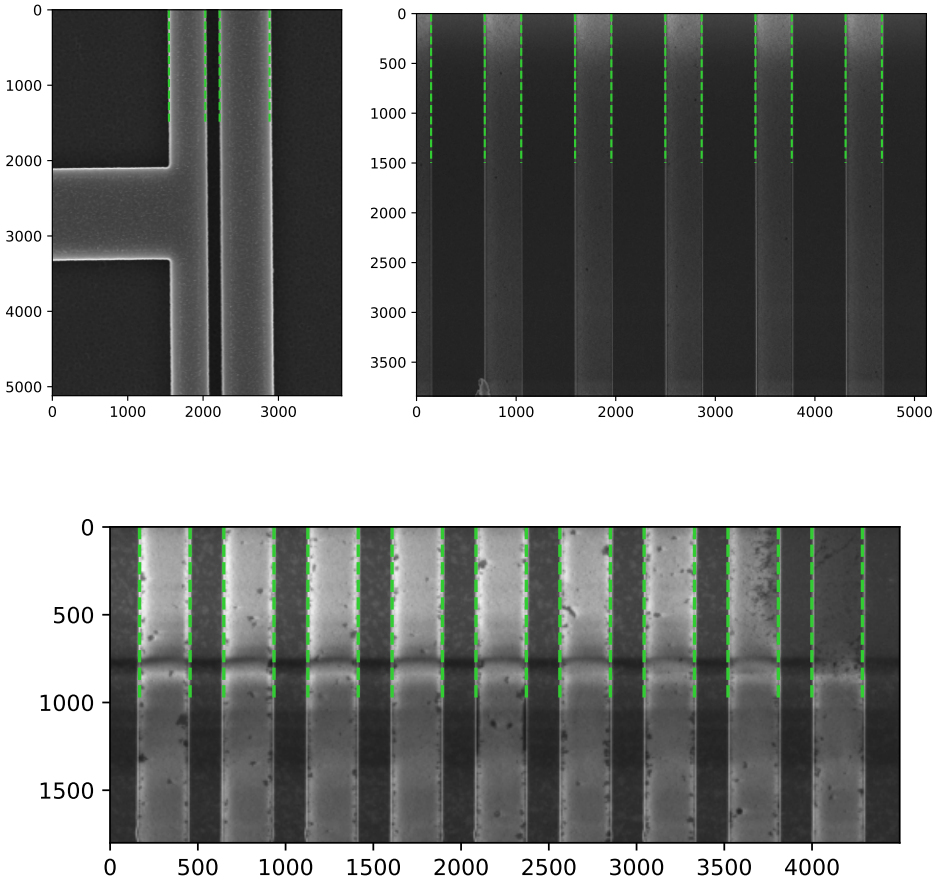

Figure A.1: SEM images of three different samples used to calculate fabrication tolerances. Top left shows an image taken of the DESHIMA filter bank, top right shows an IDC of our LT343 KID array fabricated with E-beam lithography and the bottom shows an IDC of the LT192 array fabricated with EUV lithography. Green dashed lines are used to indicate the edges found by the algorithm described in chapter 4

B

Trimming Algorithm Source Code

The full repository containing all code used for the writing of this thesis can be found on GitHub

```
1
2  def create_trim_groups(f0_measured, IDs_measured, cutoff_freq):
3
4      #Make sure all units are in Hertz
5      if f0_measured[0] < 1e7:
6          f0_measured = np.asarray(f0_measured)*1e9
7      if cutoff_freq < 1e7:
8          cutoff_freq = cutoff_freq * 1e9
9
10     #Ignore left-most part of array as control group
11     IDs_control_group = []
12     f0_control_group =[]
13     L_fabicated_control_group = []
14
15     f0_trim_group = []
16     IDs_trim_group = []
17     L_fabicated_trim_group = []
18
19     for i in range(len(f0_measured)):
20         if f0_measured[i] < cutoff_freq:
21             IDs_control_group.append(IDs_measured[i])
22             f0_control_group.append(f0_measured[i])
23             L_fabicated_control_group.append(L_design_sim[i])
24         else:
25             IDs_trim_group.append(IDs_measured[i])
26             f0_trim_group.append(f0_measured[i])
27             L_fabicated_trim_group.append(L_design_sim[i])
28
29     return f0_control_group, f0_trim_group, IDs_control_group, IDs_trim_group,
           L_fabicated_control_group, L_fabicated_trim_group
30
31
32 cutoff_freq = 5.1
33 # L_design_sim = sorted(L_design_sim, reverse=True)
34
35 freqs_control_group, freqs_trim_group, control_group_IDs, trim_group_IDs,L_fab_control_group
       ,L_fab_trim_group = create_trim_groups(freqs_pks, measured_IDs, cutoff_freq)
36
37 print(control_group_IDs)
38 print(trim_group_IDs)
39 print(freqs_pks[-1], freqs_trim_group[-1])
40 print(freqs_pks[1], freqs_control_group[1])
41
42 print(freqs_trim_group)
43 freqs_control_group_sorted = np.sort(freqs_control_group)
44
45 dL_offset = 80e-3 #Trim to account for small fabrication factor in um
```

```
46
47 def calc_offset(f0_measured, f0_simulated, L_produced ,L_simulated, dL):
48     #Make sure all units are in Hertz
49     if f0_measured[0] < 1e7:
50         f0_measured = f0_measured*1e9
51     if f0_simulated[0] < 1e7:
52         f0_simulated = f0_simulated*1e9
53
54     f0_trim = np.copy(f0_measured)
55     L_offset = np.asarray(L_produced) - dL
56     #Now to calculate new f0 for offset finger length:
57
58     L_pre_trim_match = []
59     L_post_trim_match = []
60     f0_pre_trim_match = []
61     f0_post_trim_match = []
62     pre_trim_match_index = []
63     post_trim_match_index = []
64
65     for i in range(len(f0_measured)):
66         if L_offset[i] != L_produced[i]:
67             f0_pre_trim_match_index = np.argmin(np.abs(f0_measured[i]-f0_simulated))
68             pre_trim_match_index.append(f0_pre_trim_match_index)
69             L_pre_trim_match.append(L_simulated[f0_pre_trim_match_index])
70             L_old = L_simulated[f0_pre_trim_match_index]
71             f0_pre_trim_match.append(f0_simulated[f0_pre_trim_match_index])
72
73             L_new = L_old - dL
74             L_post_trim_match_index = np.argmin(np.abs(L_new-L_simulated))
75             post_trim_match_index.append(L_post_trim_match_index)
76             L_post_trim_match.append(L_simulated[L_post_trim_match_index])
77             f0_post_trim_match.append(f0_simulated[L_post_trim_match_index])
78
79
80     print(len(f0_pre_trim_match), len(f0_post_trim_match))
81     df_trim = np.asarray(f0_post_trim_match) - np.asarray(f0_pre_trim_match)
82     f0_offset = f0_measured + df_trim
83
84     print(f"example: right most KID has been trimmed from {min(L_produced)} to {min(L_offset)
       } um")
85     print(f"example: KID has moved by {max(f0_offset - f0_measured)/1e6} MHz")
86     return f0_offset, L_offset
87
88 freqs_trim_offset, L_trim_offset = calc_offset(freqs_trim_group, freqs_dense,
       L_fab_trim_group, LF_fit_dense, dL_offset)
89
90 freqs_offset = np.hstack((freqs_control_group, freqs_trim_offset))
91 L_offset = np.hstack((L_fab_control_group, L_trim_offset))
92
93 print(trim_group_IDs[1], freqs_trim_offset[1])
94
95 df0_min =7e6
96 f0_max = 8.4e9
97 dL_offset = 80e-3 #Trim to account for small fabrication factor in um
98
99
100 f0_sorted = np.sort(freqs_trim_offset)
101 f0_sorted_index = np.argsort(freqs_trim_offset)
102 trim_group_IDs_sorted = np.asarray(trim_group_IDs)[f0_sorted_index]
103
104 def calc_capacitor_trim_freqs(df0_min, f0_max, f0_measured, f0_simulated, KID_IDs):
105
106     #Make sure all units are in Hertz
107     if f0_measured[0] < 1e7:
108         f0_measured = f0_measured*1e9
109     if f0_simulated[0] < 1e7:
110         f0_simulated = f0_simulated*1e9
111     if f0_max < 1e7:
112         f0_max = f0_max*1e9
113
114     df_array = np.array(f0_measured[1:]) - np.array(f0_measured[:-1])
```

```
115
116     print(f"initial␣left␣most␣KID␣has␣f␣=␣{f0_measured[0]/1e9}␣GHz")
117     print(f"initial␣right␣most␣KID␣has␣f␣=␣{f0_measured[-1]/1e9}␣GHz")
118     print(f"initial␣least␣distance␣f␣=␣{np.min(df_array)/1e6}␣MHz␣for␣KID␣{KID_IDs[np.argmin(
            df_array)]}␣at␣{f0_measured[np.argmin(df_array)]/1e9}␣GHZ")
119
120     KID_count = len(f0_measured)
121
122     #Simple algorithm to ensure minimum frequency-spacing, f0_trim is the proposed new list
            of resonance frequencies
123     f0_trim = np.copy(f0_measured)
124     for i in range(0,len(df_array)):
125         if df_array[i]<df0_min:
126             KID_count = KID_count - 1
127             f0_trim[i+1] = f0_trim[i] + 7.5e6
128             df_array =  f0_trim[1:] - f0_trim[:-1]
129
130     print(f"initial␣yield␣=␣{KID_count/len(f0_measured)}␣\n")
131
132     #Check for "flipped KIDs" due to nibbling and calculate new yield
133     for i in range(len(f0_measured[:-1])):
134         if f0_trim[i] > f0_trim[i+1]:
135             print(f"KID␣{i}␣switched␣with␣KID␣{i+1}")
136
137     return f0_trim
138
139 step_f0_trim = calc_capacitor_trim_freqs(df0_min, f0_max, f0_sorted, freqs_dense,
        trim_group_IDs_sorted)
140
141 final_freqs = np.hstack((freqs_control_group_sorted, step_f0_trim))
142
143 def calc_capacitor_fit(f0_trim, f0_measured, f0_simulated, L_simulated, KID_IDs):
144     #Make sure all units are in Hertz
145     if f0_measured[0] < 1e7:
146         f0_measured = f0_measured*1e9
147     if f0_simulated[0] < 1e7:
148         f0_simulated = f0_simulated*1e9
149     #Now to calculate new finger length:
150     df_trim = []
151     L_fingers_pre_trim_match = []
152     L_fingers_post_trim_match = []
153     f0_pre_trim_match = []
154     f0_post_trim_match = []
155     trimmed_KID_IDs = []
156     trim_nr = []
157     pre_trim_match_index = []
158     post_trim_match_index = []
159
160     for i in range(len(f0_measured)):
161         if f0_trim[i] != f0_measured[i]:
162             df_trim.append(f0_trim[i] - f0_measured[i])
163             f0_pre_trim_match_index = np.argmin(np.abs(f0_measured[i]-f0_simulated))
164             pre_trim_match_index.append(f0_pre_trim_match_index)
165             f0_pre_trim_match.append(f0_simulated[f0_pre_trim_match_index])
166             L_fingers_pre_trim_match.append(L_simulated[f0_pre_trim_match_index])
167             trim_nr.append(i)
168             trimmed_KID_IDs.append(KID_IDs[i])
169
170     for i in trim_nr:
171         f0_post_trim_match_index = np.argmin(np.abs(f0_trim[i]-f0_simulated))
172         post_trim_match_index.append(f0_post_trim_match_index)
173         f0_post_trim_match.append(f0_simulated[f0_post_trim_match_index])
174         L_fingers_post_trim_match.append(L_simulated[f0_post_trim_match_index])
175
176     trimmed_KID_IDs = [int(x) for x in trimmed_KID_IDs]
177     return L_fingers_pre_trim_match, f0_pre_trim_match, L_fingers_post_trim_match,
            f0_post_trim_match, pre_trim_match_index,post_trim_match_index,trimmed_KID_IDs,
            trim_nr
178
179 L_fingers_pre_trim_match, f0_pre_trim_match, L_fingers_post_trim_match, f0_post_trim_match,
        pre_trim_match_index, post_trim_match_index, ID_step,tr_nr  = calc_capacitor_fit(
```

```
    step_f0_trim, f0_sorted, freqs_dense, LF_fit_dense, trim_group_IDs_sorted)

def calc_capacitor_yield(f0_max, f0_trim, f0_measured, trimmed_KID_IDs, trim_nr, dL_offset):
#Calculate finger length to trim INCLUDING the offset we use for all KIDs anyway
    dL_trim = (np.array(L_fingers_pre_trim_match)-np.array(L_fingers_post_trim_match)) +
        dL_offset

    #create new trimmed array
    f0_array_post_trim = np.copy(f0_measured)
    f0_array_post_trim[trim_nr] = f0_post_trim_match
    df0_array_post_trim = f0_array_post_trim[1:] - f0_array_post_trim[:-1]


    #Now check if the resulting trimmed array satisfies the design requirements:
    if any(f0_trim)>f0_max:
        print("Error: Resonance frequency found outside allowed bandwidth")

    KID_count_post_trim = len(f0_measured)
    for i in range(len(df0_array_post_trim)):
        if df0_array_post_trim[i] < df0_min:
            KID_count_post_trim = KID_count_post_trim - 1

    print(f"Trimmed left most KID has f = {f0_trim[0]/1e9} GHz")
    print(f"Trimmed right most KID has f = {f0_trim[-1]/1e9} GHz")
    print(f"Trimmed least distance df = {np.min(df0_array_post_trim)/1e6} MHz for KID {
        trimmed_KID_IDs[np.argmin(df0_array_post_trim)]} at {f0_trim[np.argmin(
        df0_array_post_trim)]/1e9} GHZ")
    print(f"Trimmed yield = {KID_count_post_trim/len(f0_measured)}\n")

    print(f"In total {len(trimmed_KID_IDs)} KIDs will be variably trimmed")

    return dL_trim

dL_trim = calc_capacitor_yield(f0_max, step_f0_trim, f0_sorted, ID_step, tr_nr, dL_offset)
```